

This is the post print that has been accepted for publication by Geophysical Journal International:

Shane Zhang, Hongda Wang, Mengyu Wu, Michael H Ritzwoller, **Isotropic and azimuthally anisotropic Rayleigh wave dispersion across the Juan de Fuca and Gorda plates and U.S. Cascadia from earthquake data and ambient noise two- and three-station interferometry**, Geophysical Journal International, Volume 226, Issue 2, August 2021, Pages 862–883, <https://doi.org/10.1093/gji/ggab142>

Please feel free to contact any of the authors; we welcome feedback.

1 Introduction

Large earthquakes ($M_w \geq 8$) have recurred in Cascadia with a period of ~ 500 years over the last 10,000 years (e.g. Atwater, 1987; Goldfinger et al., 2012), and the most recent one is dated to the 1700s (e.g. Nelson et al., 1995; Satake et al., 1996). Motivated by the capability of $M_w \sim 9$ earthquakes on the Cascadia subduction zone, the Cascadia Initiative (CI, Toomey et al., 2014) deployed an array of ocean-bottom seismographs (OBS) and land stations spanning from the Juan de Fuca and Gorda Ridges onto the continent in the northwestern U.S. The CI array also provides an opportunity to image the Juan de Fuca Plate from formation to subduction, which may shed light on the thermal state, hydration and melt extent of the oceanic plate (e.g. Tian et al., 2013; Bell et al., 2016; Eilon and Abers, 2017; Rychert et al., 2018; Ruan et al., 2018; Janiszewski et al., 2019), cooling (e.g. Byrnes et al., 2017; Janiszewski et al., 2019) and deformation (e.g. Martin-Short et al., 2015; Bodmer et al., 2015; VanderBeek and Toomey, 2017; VanderBeek and Toomey, 2019) of the oceanic lithosphere, structure of the Locked and Transition Zones along the Cascadia margin (e.g. Hawley et al., 2016; Bodmer et al., 2018), and subduction of the oceanic plate (e.g. Janiszewski and Abers, 2015; Gao, 2016; Hawley and Allen, 2019). Furthermore, structural studies can provide constraints for hazard analysis, such as using the downdip limits of the subducted plate to constrain how close source zones are to metropolitan areas (Hyndman and Wang, 1993).

Classical two-station interferometry (e.g. Campillo and Paul, 2003; Shapiro and Campillo, 2004) extracts information about the medium between two synchronous receivers, which leads to ambient noise tomography (e.g. Shapiro et al., 2005; Sabra et al., 2005). In contrast, three-station interferometry (e.g. Stehly et al., 2008; Curtis and Halliday, 2010), based on two-station interferograms, additionally can bridge *asynchronously* deployed receivers (e.g. Ma and Beroza, 2012; Curtis et al., 2012), which has recently been exploited for surface wave tomography (e.g. Spica et al., 2016; Chen and Saygin, 2020; Zhang et al., 2020). Furthermore, three-station direct-wave interferometry is shown to have the theoretical advantage of reduced sensitivity to noise source distribution (Liu, 2020) and the practical advantage of improvement in Rayleigh wave dispersion measurements (Zhang et al., 2020), and potentially may be useful in this noisier amphibious setting. In addition, previous studies predominantly use earthquake body waves to observe azimuthal anisotropy on the Juan de Fuca and Gorda Plates (e.g. Martin-Short et al., 2015; Bodmer et al., 2015; VanderBeek and Toomey, 2017; VanderBeek and Toomey, 2019) and azimuthal anisotropy appears challenging to observe from earthquake-generated surface waves (e.g. Bell et al., 2016; Eilon and Forsyth, 2020).

Our two principal purposes of this study are (1) to investigate the performance of three-station direct-wave interferometry and (2) to produce Rayleigh wave isotropic and azimuthal anisotropy observations from both earthquakes and ambient noise across the Juan de Fuca and Gorda plates extending onto the continent. We use the CI array and some regional seismic networks for Rayleigh wave observations from two-station

71 interferometry, three-station interferometry, and earthquake data. The final product
72 is a set of Rayleigh wave azimuthally anisotropic phase speed maps across Cascadia
73 combining ambient noise and earthquake observations.

74 First, three-station direct-wave interferometry has been tested in the western U.S.
75 and is found to produce higher SNR dispersion measurements, to bridge asynchronously
76 deployed stations, and to derive isotropic phase speed maps consistent with two-station
77 interferometry (Zhang et al., 2020). However, the quality of two-station interferograms
78 there is already quite high. Thus, we address the extent of improvement from three-
79 station interferometry in this noisier amphibious setting with less ideal station geometry.
80 Moreover, we test if azimuthal anisotropy observations from three-station interferometry
81 are also consistent with two-station interferometry. To validate the noise-based results,
82 we introduce earthquake data as independent observations. Janiszewski et al. (2019)
83 find significant discrepancies ($> 3\%$) in Rayleigh wave isotropic phase speed maps across
84 Cascadia derived from two-station interferometry and earthquakes, especially near the
85 coastline (some locations $> 10\%$). As we will show, differences between earthquake
86 and noise-based results are reduced ($< 1\%$) by using a different methodology, especially
87 after denoising OBS data.

88 Second, to date azimuthal anisotropy on the Juan de Fuca and Gorda Plates has
89 been predominantly observed from earthquake body waves (e.g. Martin-Short et al.,
90 2015; Bodmer et al., 2015; VanderBeek and Toomey, 2017; VanderBeek and Toomey,
91 2019) and appears challenging to observe from earthquake surface waves (Bell et al.,
92 2016; Eilon and Forsyth, 2020). We show robust observations of azimuthal anisotropy
93 from earthquake surface waves based on eikonal (Lin et al., 2009) and Helmholtz tomog-
94 raphy (Lin and Ritzwoller, 2011b). We also present Rayleigh wave azimuthal anisotropy
95 measurements and tomographic maps from ambient noise two- and three-station inter-
96 ferometry which, to the best of our knowledge, have not been produced offshore. In
97 obtaining the 2ψ azimuthal anisotropy results, we pay attention to observing and cor-
98 recting for the effect of apparent 1ψ azimuthal anisotropy, which may be caused by
99 strongly heterogeneous isotropic structures and may bias 2ψ anisotropy measurements
100 (e.g. Lin and Ritzwoller, 2011a).

101 The paper is structured as follows. First, we describe the processing of data for am-
102 bient noise two-station and three-station direct-wave interferometry and for earthquake
103 observations, including the denoising of OBS data and the de-biasing of three-station
104 interferometry (**section 2**). Then, we measure Rayleigh wave dispersion from the dif-
105 ferent methods and compare their characteristics, contrasting the quality of measure-
106 ments based on OBS and land stations (**section 3**). Next, we quantify the differences in
107 the phase speed maps from the different methods utilizing the estimated uncertainties
108 (**section 4**). Finally, by combining results from the different methods we construct
109 composite maps for both isotropic and azimuthally anisotropic structure (**section 5**).

110 2 Data processing

111 The stations used in this work extend from the Juan de Fuca and Gorda Ridges onto
 112 the continent in the northwestern U.S. The resulting station set has an average spacing
 113 of ~ 70 km (**Fig. 1a**). The total number of stations is 612 with 41% (252) Ocean Bottom
 114 Seismographs (OBS) and 59% (360) land stations. The stations are largely composed
 115 of the oceanic and the continental components of the Cascadia Initiative (CI). The CI
 116 OBS deployment is divided into four yearly phases from 2011-2014: most OBS are on
 117 the Juan de Fuca Plate in 2011 and 2013 while most are on the Gorda Plate in 2012
 118 and 2014. The CI OBS are augmented with limited term deployments of OBS near
 119 the Blanco Transform Fault (2012 to 2013, Nabelek and Braunmiller, 2012) and on the
 120 Gorda Plate (2013 to 2015, Nabelek and Braunmiller, 2013). About 44% (157) of land
 121 stations are from the USArray Transportable Array (TA), most of which are deployed
 122 from 2005 to 2008 and are asynchronous with the CI stations.

123 Problematic stations are identified using travel time and amplitude information,
 124 many unidentified by previous studies (e.g. Janiszewski et al., 2019). First, ambient
 125 noise travel time residuals are computed between a priori phase speed maps (e.g. **Fig.**
 126 **13**) and measurements, and instruments with π phase shift, mislocation, or unknown
 127 errors are identified (e.g. **Fig. S1**). Second, by comparing amplitudes from the same
 128 earthquake at nearby stations, instrument gain problems are detected (e.g. **Fig. S2**). A
 129 complete list of anomalous stations is presented in the supplementary material (**Table**
 130 **S1**).

131 2.1 Ambient noise data

132 To obtain information about the medium between two receivers, we apply both two-
 133 station ambient noise interferometry (e.g. Shapiro and Campillo, 2004; Shapiro et al.,
 134 2005) as well as three-station interferometry (e.g. Stehly et al., 2008; Curtis and Halli-
 135 day, 2010; Zhang et al., 2020). We refer to interferograms from these methods generally
 136 as noise-based data, although three-station methods considered here primarily utilize
 137 the direct-wave part of two-station interferograms. In addition to cross-correlation,
 138 data processing to construct two-station interferograms includes denoising OBS data to
 139 reduce tilt and compliance noise, and temporal and spectral normalizations to reduce
 140 effects from uneven noise source distributions (**section 2.1.1**). Additionally, computa-
 141 tion of three-station interferograms requires particular attention to choosing appropriate
 142 weights for each source-station, selecting either correlation or convolution depending on
 143 station geometry, and de-biasing to produce correct dispersion measurements (**section**
 144 **2.1.2**).

145 The following is a summary of the notation used to describe the various interfero-
 146 metric methods (Zhang et al., 2020) used in this study:

- 147 • \mathcal{I}_2^{AN} : Two-station ambient noise interferometry.

- 148 • $ell\mathcal{I}_3^{DW}$: Three-station direct-wave interferometry with source-stations in the el-
149 liptical stationary phase zone between the receiver stations.
- 150 • $hyp\mathcal{I}_3^{DW}$: Three-station direct-wave interferometry with source-stations in the hy-
151 perbolic stationary phase zones radially outside the receiver stations.

152 2.1.1 Two-station interferometry

153 For \mathcal{I}_2^{AN} , the preprocessing of continuous data is performed in two major steps.
154 First, we reduce tilt and compliance noise from vertical components of OBS using the
155 horizontal components and the pressure gauges, respectively (e.g. Webb and Crawford,
156 1999; Crawford and Webb, 2000; Bell et al., 2015; Tian and Ritzwoller, 2017), in a
157 process we refer to as “denoising”. The denoising is particularly impactful at periods
158 > 10 s and for shallow water OBS (Tian and Ritzwoller, 2017). Second, we apply
159 traditional ambient noise pre-processing steps including temporal and spectral normal-
160 izations (e.g. Bensen et al., 2007; Ritzwoller and Feng, 2019) to reduce the effects of
161 strong directionally-dependent sources (such as earthquakes). Then the data are corre-
162 lated and stacked over days to produce correlations between all synchronously deployed
163 station-pairs. The correlations from nearby stations (distance < 0.5 km) are simply
164 superimposed (stacked), whether the stations are deployed synchronously or not. Fi-
165 nally, we average the causal and acausal lags of the correlations to form the symmetric
166 component, which we also use as the basis for three-station interferometry (**section**
167 **2.1.2**) and for tomography based on two-station interferometry (**section 4**).

168 2.1.2 Three-station interferometry

169 We first summarize the essentials of the three-station methods used in this study
170 (**Fig. 2**) because three-station interferometric methods are currently less well estab-
171 lished than two-stations methods. Zhang et al. (2020) presents the methods, notation,
172 and terminology in detail. Consider three stations at a time, and denote two of them
173 as receiver-stations, r_i, r_j , and the third as a source-station, s_k . The two two-station
174 interferograms between s_k and r_i as well as s_k and r_j individually are correlated or
175 convolved again to produce a source-specific three-station interferogram, $C_3(r_i, r_j; s_k)$,
176 where C represents either correlation or convolution and the dependence on time is sup-
177 pressed here. Then the source-specific interferograms are phase shifted and stacked over
178 N source-stations with appropriate weights, $w_{ij;k}$, to produce the composite estimated
179 Green’s function, \hat{G}_3 , between receiver-stations r_i and r_j :

$$\hat{G}_3(r_i, r_j) \equiv \sum_{k=1}^N w_{ij;k} \tilde{C}_3(r_i, r_j; s_k), \quad (1)$$

180 where \tilde{C}_3 denotes the interferogram C_3 after a “de-biasing” phase shift is applied. \hat{G}_3
 181 provides information about the medium between receiver-stations r_i and r_j , which may
 182 be deployed asynchronously. Each weight w (indices suppressed) can be decomposed
 183 into three factors:

$$w = \mathbf{1}_{\text{geometry}} \cdot \mathbf{1}_{\text{SNR}} \cdot w_{\text{RMS}}, \quad (2)$$

184 where $\mathbf{1}_{\text{geometry}}$ is an indicator function that is 1 if s_k satisfies a particular geometrical
 185 constraints and 0 otherwise, $\mathbf{1}_{\text{SNR}}$ is also an indicator function that is 1 only if the SNR
 186 of both $\mathcal{I}_2(r_i, s_k)$ and $\mathcal{I}_2(r_j, s_k)$ are > 10 . SNR is defined as the ratio between the peak
 187 amplitude in the signal window and the RMS of trailing noise (Bensen et al., 2007)
 188 throughout this study. w_{RMS} equals the reciprocal of the RMS of the trailing noise in
 189 the interferogram \tilde{C}_3 , which normalizes amplitudes of \tilde{C}_3 while accentuating \tilde{C}_3 with
 190 high SNR.

191 The most fundamental component of the weight function is the geometrical weight,
 192 $\mathbf{1}_{\text{geometry}}$, which requires source-stations to lie within stationary phase zones (Fig. 2,
 193 Snieder (2004)). To define the stationary phase zones, let d denote the great-circle
 194 distance between two stations, then let ${}^{\text{hyp}}\delta d$ represent the difference between the dif-
 195 ferential source-receiver distances and the inter-receiver distance (Fig. 2a):

$${}^{\text{hyp}}\delta d_{ij;k} = |d_{ki} - d_{kj}| - d_{ij}, \quad (3)$$

196 and let ${}^{\text{ell}}\delta d$ represent the difference between the sum of source-receiver distances and
 197 the inter-receiver distance (Fig. 2b):

$${}^{\text{ell}}\delta d_{ij;k} = |d_{ki} + d_{kj}| - d_{ij}, \quad (4)$$

198 corresponding to the methods ${}^{\text{hyp}}\mathcal{I}_3^{\text{DW}}$ and ${}^{\text{ell}}\mathcal{I}_3^{\text{DW}}$, respectively. Because of the triangle
 199 inequality, ${}^{\text{hyp}}\delta d \leq 0$ while ${}^{\text{ell}}\delta d \geq 0$. For both ${}^{\text{hyp}}\mathcal{I}_3^{\text{DW}}$ and ${}^{\text{ell}}\mathcal{I}_3^{\text{DW}}$, the stationary phase
 200 zones are *ad hoc* defined as

$$|\delta d_{ij;k}| < \alpha \cdot d_{ij}, \quad (5)$$

201 with appropriate left superscripts for δd in eqs. (3) and (4), and we empirically choose
 202 $\alpha = 1\%$. Strictly speaking, the term “stationary phase zone” refers to the first Fresnel
 203 zone (typically defined as $\delta d \leq \frac{\lambda}{n}$, where λ is the wavelength at a certain period and
 204 n is a constant) and should depend on frequency. The stationary phase zone referred
 205 to in this study (eq. (5)) is narrower than the (first) Fresnel zone and is frequency
 206 independent. For ${}^{\text{ell}}\mathcal{I}_3^{\text{DW}}$, the stationary phase zone is an ellipse, and $\mathcal{I}_2(r_i, s_k)$ and
 207 $\mathcal{I}_2(r_j, s_k)$ are convolved. For ${}^{\text{hyp}}\mathcal{I}_3^{\text{DW}}$, the stationary phase zone is a hyperbola, and
 208 $\mathcal{I}_2(r_i, s_k)$ and $\mathcal{I}_2(r_j, s_k)$ are correlated. Because signals in $\mathcal{I}_2^{\text{AN}}$ become unreliable for
 209 inter-station distances less than one wavelength λ , we also require both source-receiver
 210 distances to be greater than λ . For simplicity, but without rejecting too many source-
 211 stations, we use a cutoff wavelength at the longest period of interest:

$$\min(d_{ki}, d_{kj}) > \lambda_{\text{max}}, \quad (6)$$

212 where $\lambda_{\max} = 120$ km for a period of 40 s and an approximate wave speed of 3 km/s.

213 Without accounting for δd , the dispersion measurements will be biased in both
 214 group speed (Chen and Saygin, 2020) and phase speed (Zhang et al., 2020). Zhang et
 215 al. (2020) presents a de-biasing scheme to measure the dispersion of each source-specific
 216 interferogram (C_3) individually with the corrected distance, $d_{ij} + \delta d_{ij;k}$. Then the
 217 source-specific dispersion curves are averaged over source-stations s_k with the standard
 218 deviation as an estimate of uncertainty. Here, in contrast, we present a new de-biasing
 219 approach in which we apply a phase shift to each original C_3 in the frequency domain:

$$\tilde{C}_3 = \mathcal{F}^{-1} \left[\mathcal{F}[C_3] \cdot e^{i\omega\delta d/c} \right], \quad (7)$$

220 where \mathcal{F} and \mathcal{F}^{-1} denote the Fourier transform and its inverse, respectively, and c is
 221 an input estimate of phase speed between the receiver-stations. The dependence of C_3
 222 and \tilde{C}_3 on r_i, r_j, s_k and time is suppressed for clarity in the preceding equation. **Fig.**
 223 **3** shows an example of the effect of the phase shift for station triplets with different
 224 values of δd . For the method $^{hyp}\mathcal{I}_3^{DW}$ a phase delay is applied because $^{hyp}\delta d \leq 0$, while
 225 for the method $^{ell}\mathcal{I}_3^{DW}$ a phase advance is applied because $^{ell}\delta d \geq 0$.

226 The major difference in the three-station methods between this work and Zhang
 227 et al. (2020) is that here we apply a phase shift to de-bias. The main advantage of the
 228 phase shift approach is to preserve the stack of source-specific interferograms (\hat{G}_3), which
 229 is designed to produce more reliable dispersion measurements with broader bandwidth
 230 than the individual C_3 . However, application of the phase shift requires prior knowledge
 231 of the phase speed, although the process can be iterated. In this study, we use prior
 232 information from phase speed maps constructed using \mathcal{I}_2^{AN} . Because we find the de-
 233 biasing effective (**section 4.1**), we do not iteratively update the phase speed map and
 234 re-apply the correction.

235 In Zhang et al. (2020), three-station coda-wave interferometry (e.g. Stehly et al.,
 236 2008) is also investigated and is found to produce lower SNR and more band-limited
 237 measurements than the methods \mathcal{I}_2^{AN} , $^{ell}\mathcal{I}_3^{DW}$ and $^{hyp}\mathcal{I}_3^{DW}$. In fact, we find coda-wave
 238 interferometry even more challenging in this noisy oceanic setting, so we do not present
 239 results from it here. Hence, when we refer to three-station methods here, we will mean
 240 three-station *direct-wave* interferometry.

241 2.2 Earthquake data

242 More than 2500 teleseismic earthquakes with $M_s > 5.5$ are used (**Fig. 1b**) to pro-
 243 duce Rayleigh wave dispersion measurements. The earthquakes are widely distributed
 244 in azimuth with a predominant fraction from the western Pacific, which can provide
 245 complementary azimuthal coverage to noise-based data (**section 4**). Preprocessing of
 246 earthquake data recorded on OBS includes reducing tilt and compliance noise, similar
 247 to the denoising of ambient noise data recorded on OBS (**section 2.1.1**).

248 3 Dispersion measurements

249 We apply frequency-time analysis (e.g. Dziewonski et al., 1969; Levshin and Ritz-
 250 woller, 2001) to measure Rayleigh wave phase speed, assuming the instantaneous phase
 251 of the signal at frequency ω and time t to be (e.g. Lin et al., 2008):

$$\phi(\omega, t) = \omega \frac{d}{c} - \omega t + \frac{\pi}{4} + 2N\pi + \phi_s, \quad (8)$$

252 where d is the inter-receiver distance, c is the phase speed we wish to measure, $N \in \mathbb{Z}$,
 253 and ϕ_s is a source-dependent term. As discussed in detail by Zhang et al. (2020), an ap-
 254 propriate ϕ_s must be chosen to obtain approximately unbiased dispersion measurements
 255 for the different methods we consider here:

$$\phi_s = \begin{cases} 0 & \text{for } \mathcal{I}_2^{\text{AN}}, \\ \pi/4 & \text{for } {}^{\text{ell}}\mathcal{I}_3^{\text{DW}}, \\ -\pi/4 & \text{for } {}^{\text{hyp}}\mathcal{I}_3^{\text{DW}}. \end{cases} \quad (9)$$

256 For earthquake data, ϕ_s will depend on source parameters and frequency, but here we
 257 simply choose $\phi_s = 0$ because only unbiased travel time *differences* are used in the
 258 tomography methods applied in this study (section 4). Differencing of phase travel
 259 time measurements approximately cancels the initial phase term. We also resolve 2π
 260 ambiguity for each earthquake by iteratively applying corrections to stations in order
 261 of increasing distance from the center station (Lin and Ritzwoller, 2011b). Similarly,
 262 one could also choose any constant as ϕ_s for the methods $\mathcal{I}_2^{\text{AN}}$, ${}^{\text{ell}}\mathcal{I}_3^{\text{DW}}$, and ${}^{\text{hyp}}\mathcal{I}_3^{\text{DW}}$ to
 263 perform tomography, although the dispersion measurements would be biased. Earth-
 264 quake dispersion measurements from the TA stations are based on Shen and Ritzwoller
 265 (2016).

266 The source strengths with ambient noise and data quality can be cumulatively char-
 267 acterized by SNR. **Fig. 4a** shows the median of SNR versus period from all paths. On
 268 average, the SNR for the three-station measurements are about 50% higher than for
 269 the two-station measurements. SNR values are similar between the methods ${}^{\text{ell}}\mathcal{I}_3^{\text{DW}}$ and
 270 ${}^{\text{hyp}}\mathcal{I}_3^{\text{DW}}$. SNR curves for ambient noise-based data peak near the primary (~ 16 s)
 271 and secondary (~ 8 s) microseisms and decay rapidly at longer periods. The primary
 272 and secondary microseisms may be generated from different mechanisms (e.g. Tian and
 273 Ritzwoller, 2015). In contrast, the SNR curve for earthquakes shows a single peak
 274 around 35 s period and remains high (> 25) at longer periods but decays rapidly at
 275 shorter periods. Therefore, ambient noise and earthquake data complement each other
 276 by providing higher SNR measurements for periods below and above 30 s, respectively.
 277 The paths for noise-based data can be divided into three categories (**Figs 4b-d**) by the
 278 type of station-pair used: “Land-Land” (between land stations), “OBS-Land” (between
 279 OBS and land stations), and “OBS-OBS” (between OBS and OBS).

280 For Land-Land paths (**Fig. 4b**), the SNR is the highest among all categories.
 281 Three-station methods ($^{ell}\mathcal{I}_3^{DW}$ and $^{hyp}\mathcal{I}_3^{DW}$) enhance SNR by an additive value of ~ 10
 282 compared with two-station interferometry (\mathcal{I}_2^{AN}), except for periods < 10 s. The en-
 283 hancement is not large because the SNR of \mathcal{I}_2^{AN} is already quite high (> 20) across a
 284 broad frequency band on land.

285 For OBS-Land paths (**Fig. 4c**), the SNR of \mathcal{I}_2^{AN} peaks near 18 s period (~ 24) and
 286 decreases quickly at shorter and longer periods (< 10 at 40 s). On average, the SNR
 287 is more than three times lower than Land-Land paths (**Fig. 4a**). Because SNR of
 288 \mathcal{I}_2^{AN} is low in the oceans, three-station methods $^{ell}\mathcal{I}_3^{DW}$ and $^{hyp}\mathcal{I}_3^{DW}$ provide substantial
 289 enhancements that nearly double the SNR of \mathcal{I}_2^{AN} .

290 For OBS-OBS paths (**Fig. 4d**), the SNR is the lowest among all categories of paths
 291 and drops quickly at periods > 12 s. SNR curves for the methods \mathcal{I}_2^{AN} and $^{ell}\mathcal{I}_3^{DW}$ are
 292 very similar at periods > 12 s whereas $^{ell}\mathcal{I}_3^{DW}$ has a lower SNR at shorter periods. SNR
 293 curves for \mathcal{I}_2^{AN} and $^{hyp}\mathcal{I}_3^{DW}$ are similar at periods < 12 s, whereas $^{hyp}\mathcal{I}_3^{DW}$ nearly doubles
 294 the SNR of \mathcal{I}_2^{AN} at longer periods. The enhancement from $^{hyp}\mathcal{I}_3^{DW}$ compared with \mathcal{I}_2^{AN} is
 295 important for obtaining more dispersion measurements as is discussed below. The
 296 method $^{hyp}\mathcal{I}_3^{DW}$ yields higher SNR than $^{ell}\mathcal{I}_3^{DW}$ because of the geometry of the methods
 297 (**Fig. 2**) and that OBS are noisier than land stations. Specifically, source-stations lie
 298 between the receiver-stations for $^{ell}\mathcal{I}_3^{DW}$, so all source-stations are OBS for OBS-OBS
 299 paths. In contrast, source-stations are in the end-fire directions for $^{hyp}\mathcal{I}_3^{DW}$, which could
 300 include land stations.

301 The quality control of the dispersion measurements includes two principal criteria.
 302 First, for both earthquake and ambient noise-based data, a spectral SNR threshold is
 303 applied that rejects a dispersion measurement at any period with SNR < 10 . This SNR
 304 criterion rejects 20% to 50% of data for \mathcal{I}_2^{AN} , 10% to 30% for $^{ell}\mathcal{I}_3^{DW}$ and $^{hyp}\mathcal{I}_3^{DW}$, and
 305 15% to 25% for earthquake data. Second, for noise-based data, a measurement at a
 306 given period is discarded if the inter-receiver distance is less than the wavelength at
 307 that period. This distance criterion only rejects a few percent of data.

308 **Figs 4e-h** show the number of paths after quality control versus period. In eikonal
 309 tomography, a single travel time measurement between two stations is used twice be-
 310 cause each station can serve as a source and a receiver. For example, a travel time
 311 measurement between stations A and B yields two paths: from station A to station
 312 B and vice versa. Therefore, for the ambient noise methods, the number of paths are
 313 twice the number of measurements. In contrast, this doubling does not affect earth-
 314 quake measurements; the number of paths and the number of travel time measurements
 315 are the same.

316 **Fig. 4e** shows the total number of paths from each method. Because SNR plays an
 317 important role in quality control, the number of paths varies with period similar to SNR
 318 (**Fig. 4a**). $^{ell}\mathcal{I}_3^{DW}$ and $^{hyp}\mathcal{I}_3^{DW}$ produce similar numbers of measurements with \mathcal{I}_2^{AN} at
 319 periods < 10 s, but provide 50% to 100% more than \mathcal{I}_2^{AN} at longer periods because
 320 of higher SNR as well as bridging asynchronously deployed stations. At long periods,

321 earthquake data provide complementary paths to noise-based data. For this part of the
 322 discussion, we continue to label paths from noise-based data into three categories by
 323 whether OBS or land stations are involved as in **Figs 4b-d**.

324 For the Land-Land category (**Fig. 4f**), the method $^{ell}\mathcal{I}_3^{DW}$ produces a similar num-
 325 ber of measurements to \mathcal{I}_2^{AN} while the method $^{hyp}\mathcal{I}_3^{DW}$ produces $\sim 20\%$ more paths at
 326 periods > 10 s. The method $^{hyp}\mathcal{I}_3^{DW}$ produces more measurements than $^{ell}\mathcal{I}_3^{DW}$ although
 327 their SNR's are similar (**Fig. 4b**), indicating that the station configuration is preferable
 328 for $^{hyp}\mathcal{I}_3^{DW}$. The Land-Land category composes 30% to 40% of all paths.

329 For the OBS-Land category (**Fig. 4g**), the methods $^{ell}\mathcal{I}_3^{DW}$ and $^{hyp}\mathcal{I}_3^{DW}$ produce
 330 $\sim 50\%$ and $\sim 80\%$ more measurements than \mathcal{I}_2^{AN} , respectively. The method $^{ell}\mathcal{I}_3^{DW}$ yields
 331 more measurements than $^{hyp}\mathcal{I}_3^{DW}$ although their SNR's are comparable (**Fig. 4c**), in-
 332 dicating that the station geometry is more advantageous for $^{ell}\mathcal{I}_3^{DW}$. About 50% of all
 333 paths are from the OBS-Land category.

334 For the OBS-OBS category (**Fig. 4h**), the method $^{ell}\mathcal{I}_3^{DW}$ produces a similar number
 335 of measurements as \mathcal{I}_2^{AN} while $^{hyp}\mathcal{I}_3^{DW}$ produces several times more at periods > 10 s.
 336 The method $^{hyp}\mathcal{I}_3^{DW}$ yields more measurements than $^{ell}\mathcal{I}_3^{DW}$ because of much higher
 337 SNR (**Fig. 4d**). As discussed above, $^{hyp}\mathcal{I}_3^{DW}$ has higher SNR because of the geomet-
 338 rical constraints on the methods such that more land source-stations are included in
 339 this category for $^{hyp}\mathcal{I}_3^{DW}$ than for $^{ell}\mathcal{I}_3^{DW}$, and land stations have better signal quality
 340 than OBS. The OBS-OBS category constitutes the least of all paths among the three
 341 categories ($< 15\%$).

342 4 Comparing results from different methods

343 Combining the different types of data from different methods (two- and three-station
 344 interferograms, earthquake measurements) promises to reduce uncertainties, to enhance
 345 azimuthal coverage, and to broaden the bandwidth. However, the combination requires
 346 the data to be mutually consistent. In this section we test the hypothesis that the results
 347 from the different methods are consistent, and present a quantitative comparison of
 348 results for both isotropic (**section 4.2**) and azimuthally anisotropic properties (**section**
 349 **4.3**). Ultimately, as we show, this comparison justifies the combination of the data sets.
 350 We discuss the composite isotropic and anisotropic phase speed maps in **section 5**.

351 4.1 Methodology, notation, and terminology

352 We perform Helmholtz tomography (Lin and Ritzwoller, 2011b) for earthquake data
 353 and eikonal tomography (Lin et al., 2009) for ambient noise data. We do not use more
 354 traditional integrated ray tomographic methods (e.g. Barmin et al., 2001) for comparing
 355 results from different data because they usually require tuning of regularization param-
 356 eters in an ad hoc way depending on the path distribution. The results from traditional
 357 methods with different numbers of measurements, therefore, are difficult to compare

358 with one another. Furthermore, Helmholtz/eikonal tomography yields local estimates
 359 of uncertainties, which are useful to guide the comparison of different methods and are
 360 crucial for studies based on phase speed maps (e.g. 3-D inversions for both isotropic
 361 and anisotropic structures).

362 A single mode and single frequency surface wave approximately satisfies the 2-D
 363 homogeneous wave equation (e.g. Lin et al., 2012). Assuming a sufficiently smooth
 364 Earth model and ignoring local amplifications, separation of variables yields:

$$\frac{1}{c_i^2(\mathbf{r})} = |\nabla\tau_i(\mathbf{r})|^2 - \frac{\nabla^2 A_i(\mathbf{r})}{\omega^2 A_i(\mathbf{r})}, \quad (10)$$

365 which uses the travel time, τ_i , and amplitude, A_i , from the i th (virtual or real) source
 366 to estimate source-specific corrected (or structural) phase speed, c_i , at the location \mathbf{r} .
 367 Helmholtz tomography is based on eq. (10) and is a finite frequency method.

368 If the amplitude field is sufficiently smooth or the frequency is high then the second
 369 term on the RHS of eq. (10) will be small compared to the first term, which produces
 370 the eikonal equation:

$$\frac{\hat{k}_i(\mathbf{r})}{c'_i(\mathbf{r})} \cong \nabla\tau_i(\mathbf{r}), \quad (11)$$

371 where \hat{k}_i is ray propagation direction and c'_i is apparent (or dynamic) phase speed.
 372 Eikonal tomography is based on eq. (11) and is a geometrical ray theoretic method.

373 In eqs. (10) and (11), we use c to denote the corrected (structural) phase speed and
 374 c' for the apparent (dynamic) phase speed. However, we do not make this distinction
 375 hereafter unless the context is ambiguous.

376 When a large number of real or virtual sources are available, phase speeds at \mathbf{r} can
 377 be binned by the azimuth of propagation. The mean and standard deviation of the
 378 mean (SDOM) in each bin are then computed (Lin et al., 2009), producing results such
 379 as those in **Fig. 5** for the 30 s Rayleigh wave at four locations based on the different
 380 methods we consider here. We then apply a least-squares fit (e.g. Tarantola, 2005)
 381 to the binned statistics, assuming that the dependence of phase speed on the azimuth
 382 (clockwise from north), ψ , is approximated by weak 2ψ anisotropy (e.g. Smith and
 383 Dahlen, 1973) and possible apparent 1ψ anisotropy (e.g. Lin and Ritzwoller, 2011a):

$$c(\psi) = \bar{c} \left(1 + \frac{A_1}{2} \cos(\psi - \psi_1) + \frac{A_2}{2} \cos 2(\psi - \psi_2) \right). \quad (12)$$

384 Here, \bar{c} is the isotropic phase speed with the “bar” denoting an average over azimuth.
 385 The anisotropic parameters are (A_1, ψ_1) , which represent the peak-to-peak relative am-
 386 plitude and the fast direction of the 1ψ component, and (A_2, ψ_2) , which are the peak-
 387 to-peak relative amplitude and the fast direction of the 2ψ component. We estimate
 388 associated uncertainties in each of the estimated quantities by standard error propaga-
 389 tion, which we denote as $\sigma_{\bar{c}}, \sigma_{A_1}, \sigma_{\psi_1}, \sigma_{A_2}$, and σ_{ψ_2} .

390 In practice, we perform tomography on a $0.2^\circ \times 0.2^\circ$ spatial grid. From 10 s period to
 391 40 s period we apply eikonal tomography to results from the ambient noise methods \mathcal{I}_2^{AN} ,
 392 $ell\mathcal{I}_3^{DW}$ and $hyp\mathcal{I}_3^{DW}$, and from 28 s period to 80 s period we use Helmholtz tomography
 393 on the earthquake data. Thus, the phase speed maps from ambient noise data and
 394 earthquake data overlap from 28 s to 40 s period. We compute isotropic phase speeds,
 395 \bar{c} , on this grid, which results in a resolution equal to about the average station spacing
 396 (~ 70 km) (Lin et al., 2009). However, to estimate azimuthal anisotropy, phase speeds
 397 from each point on the $0.2^\circ \times 0.2^\circ$ grid are combined with those from the eight neighbors
 398 to produce results on a $0.6^\circ \times 0.6^\circ$ grid, which lowers the resolution to $\sim 1.2^\circ$ or 130 km.

399 The complementarity and consistency between the different data types can be visu-
 400 alized in the local anisotropy observations. **Fig. 5** shows measurements of the azimuthal
 401 distribution of phase speed for the 30 s Rayleigh wave at several points (yellow stars in
 402 **Fig. 1a**). For example, near the Juan de Fuca Ridge (**Fig. 5(first row)**), ambient
 403 noise-based data (**Figs 5aei**) have azimuthal gaps for azimuths $\psi > 180^\circ$ because of
 404 the lack of stations toward the west, while earthquake data (**Fig. 5m**) provide com-
 405 plementary azimuths using earthquakes from the west (**Fig. 1b**). Moreover, ambient
 406 noise-based data generally have larger uncertainties from the west than from the east
 407 (**Figs 5a-l**) because OBS measurements tend to have lower signal-to-noise ratios than
 408 land stations, while earthquake data have smaller uncertainties from the west (**Figs**
 409 **5m-p**) because more earthquakes lie west of our study area (**Fig. 1b**). Thus, the com-
 410 posite data (**Figs 5q-t**) provide better azimuthal coverage than each data type alone.
 411 Estimates of 2ψ anisotropy fast directions, ψ_2 , from the different methods mostly dif-
 412 fer by $< 15^\circ$ ($< 10\%$ fractional uncertainty for the azimuthal range of 180°) while the
 413 amplitude of 2ψ anisotropy, A_2 , can differ by $> 1\%$ ($> 30\%$ fractional uncertainty for
 414 an amplitude of 3%).

To compare results from pairs of different methods, we use Welch’s unequal variances
 t -test. Assume we are comparing results from two methods denoted α and β , where α
 and β can take the values \mathcal{I}_2^{AN} , $hyp\mathcal{I}_3^{DW}$, $ell\mathcal{I}_3^{DW}$, and EQ for two-station interferometry
 (\mathcal{I}_2^{AN}), three-station interferometry ($hyp\mathcal{I}_3^{DW}$ or $ell\mathcal{I}_3^{DW}$), and earthquake tomography
 (EQ). Consider two isotropic phase speed maps computed with any two methods α and
 β , $\bar{c}_\alpha(\mathbf{r})$ and $\bar{c}_\beta(\mathbf{r})$, with associated uncertainty maps, $\sigma_{\bar{c}_\alpha}(\mathbf{r})$ and $\sigma_{\bar{c}_\beta}(\mathbf{r})$ at position \mathbf{r} .
 We then compute the following comparison statistics for the phase speeds:

$$\epsilon_{\bar{c};\alpha\beta}(\mathbf{r}) \equiv \sqrt{\sigma_{\bar{c}_\alpha}^2(\mathbf{r}) + \sigma_{\bar{c}_\beta}^2(\mathbf{r})}, \quad (13)$$

$$\Delta_{\bar{c};\alpha\beta}(\mathbf{r}) \equiv \frac{\bar{c}_\alpha(\mathbf{r}) - \bar{c}_\beta(\mathbf{r})}{\epsilon_{\bar{c};\alpha\beta}(\mathbf{r})}, \quad (14)$$

415 at location \mathbf{r} . $\epsilon_{\bar{c};\alpha\beta}(\mathbf{r})$ denotes the “combined phase speed uncertainty map” from
 416 methods α and β . $\Delta_{\bar{c};\alpha\beta}(\mathbf{r})$ is the “normalized phase speed difference map” between
 417 methods α and β . $\Delta_{\bar{c};\alpha\beta}(\mathbf{r})$ is unitless but $\epsilon_{\bar{c};\alpha\beta}(\mathbf{r})$ has the same unit as $\sigma_{\bar{c}}$ (m/s).

418 For all pairs of maps, we also compute tomography analogues to eqs. (13) and (14) for the

419 anisotropic quantities A_2 and ψ_2 : Δ_{A_2} , Δ_{ψ_2} , ϵ_{A_2} , and ϵ_{ψ_2} . Carrying along the subscripts
 420 in Δ and ϵ is cumbersome, so we suppress them wherever context can determine their
 421 values. In all cases, Δ is unitless, but ϵ_{A_2} has the same unit as A_2 (%) and ϵ_{ψ_2} has the
 422 same unit as ψ_2 (°).

For a quantity x (e.g. Δ, ϵ), we use $\langle x \rangle$ to denote its spatial mean and $\langle x^2 \rangle$ to denote
 its spatial standard deviation. For example, the spatial mean and standard deviation
 of the normalized difference between two maps, Δ , are as follows:

$$\langle \Delta \rangle \equiv \frac{1}{M} \sum_{i=1}^M \Delta(\mathbf{r}_i), \quad (15)$$

$$\langle \Delta^2 \rangle \equiv \left(\frac{1}{M} \sum_{i=1}^M (\Delta(\mathbf{r}_i) - \langle \Delta \rangle)^2 \right)^{\frac{1}{2}}, \quad (16)$$

423 where Δ is defined at M spatial grid locations.

424 $\langle \Delta \rangle$ signifies the level of systematic bias in the quantity presented on the two maps.
 425 For two maps not to be considered systematically different, $|\langle \Delta \rangle| < 1$; that is, the
 426 spatial mean of the difference is less than the average uncertainty. $\langle \epsilon \rangle$ indicates the
 427 spatially averaged uncertainty in a quantity for the two maps. Multiplying $\langle \Delta \rangle$ by
 428 $\langle \epsilon \rangle$ gives an approximate estimate of systematic bias specified with units. Also, $\langle \Delta^2 \rangle$
 429 signifies the standard deviation of the normalized difference taken over the maps. If
 430 we have estimated the uncertainties reliably then $\langle \Delta^2 \rangle \sim 1$. If $\langle \Delta^2 \rangle > 1$, then we may
 431 have underestimated the uncertainties in one or the other or both of the maps under
 432 comparison.

433 4.2 Isotropic phase speed maps

434 Examples of the estimated phase speed maps, $\bar{c}(\mathbf{r})$, and uncertainties, $\sigma_{\bar{c}}(\mathbf{r})$, pro-
 435 duced with the different methods are shown in **Fig. 6** for 30 s period. The maps are
 436 qualitatively similar to one another, with higher phase speeds in the oceanic regions
 437 (due to thinner crust) and more variable phase speeds on land. Several normalized
 438 difference maps, $\Delta_{\bar{c}}$, at 30 s period are displayed in **Fig. 7**. The patterns of the differ-
 439 ences are relatively random (**Figs 7aceg**), except the systematic differences near the
 440 Cascade Range between the \mathcal{I}_2^{AN} map and the earthquake map (**Fig 7e**). This stripe
 441 where earthquake derived phase speeds are faster than those from ambient noise has
 442 been noted before (e.g. Yang and Ritzwoller, 2008), but the discrepancy reduces as the
 443 number of earthquakes increases (e.g. Shen and Ritzwoller, 2016). Right to the west of
 444 this stripe is one smaller in area and magnitude where earthquake derived phase speeds
 445 are slower than those from ambient noise. The cause of the discrepancy remains poorly
 446 understood (e.g. Kästle et al., 2016).

447 Statistics describing the different maps are plotted in each panel of the bottom
 448 row of **Fig. 7**. For example, in the comparison between \mathcal{I}_2^{AN} and $^{hyp}\mathcal{I}_3^{DW}$ (**Figs 7cd**),

449 $\langle \Delta \rangle = 0.5$, $\langle \Delta^2 \rangle = 2.0$, and $\langle \epsilon \rangle = 11$ m/s. That is, the spatial average of the normalized
 450 difference in phase speed between these methods is 0.5, which means that \mathcal{I}_2^{AN} produces
 451 faster phase speeds at this period than $^{hyp}\mathcal{I}_3^{DW}$ by half of the average uncertainty level,
 452 which is 11 m/s. This is below the threshold, $|\langle \Delta \rangle| > 1$, for the maps to be considered
 453 systematically different. The standard deviation of the normalized difference taken
 454 over the maps, however, is 2.0. This indicates that our uncertainties for either or
 455 both of \mathcal{I}_2^{AN} and $^{hyp}\mathcal{I}_3^{DW}$ are probably underestimated. Other comparisons presented
 456 in **Fig. 7** are similar: systematic bias between the maps is below the threshold that
 457 we use to indicate the maps are significantly different but our uncertainties tend to be
 458 underestimated. Multiplying uncertainties by ~ 2 would be needed to rectify this at this
 459 period.

460 We perform similar analyses across all periods where the results of the methods
 461 overlap, and the statistics are summarized in **Fig. 8** in which we plot the spatial mean
 462 $\langle \Delta \rangle$ and standard deviation $\langle \Delta^2 \rangle$ of the normalized differences of each pair of phase
 463 speed maps along with the mean of the combined uncertainties $\langle \epsilon \rangle$.

464 The results relevant to an assessment of systematic bias between pairs of maps,
 465 which are the basis for the combination of the data from the different methods, are
 466 shown in **Fig. 8 (first row)**. The normalized bias, $\langle \Delta \rangle$, between the maps typically
 467 lies between ± 1 . The primary exception is the comparison between the $^{ell}\mathcal{I}_3^{DW}$ and
 468 $^{hyp}\mathcal{I}_3^{DW}$ methods in the narrow band between 14 and 18 s. From the general low level
 469 of systematic bias between the methods, we conclude that the maps from the different
 470 methods are consistent and, therefore, the measurements that derive from the methods
 471 can be combined.

472 One can approximately convert the systematic bias results in **Fig. 8 (first row)**
 473 from unitless to units of m/s, by multiplying by the spatially averaged combined un-
 474 certainties, $\langle \epsilon \rangle$, presented in **Fig. 8 (third row)**. These uncertainties minimize near
 475 20 s period ($\langle \epsilon \rangle \sim 10$ m/s) and increase at shorter and longer periods ($\langle \epsilon \rangle \sim 20$ m/s),
 476 which is consistent with the quality of the dispersion measurements (**Fig. 4**). An
 477 average value of bias is about $\langle \Delta \rangle = 0.5$, which when multiplied by an average value
 478 of $\langle \epsilon \rangle \sim 12$ m/s, converts to ~ 6 m/s ($\sim 0.2\%$ for a phase speed of 3 km/s), which is
 479 appropriately low.

480 The standard deviations of the normalized differences between the maps, $\langle \Delta^2 \rangle$, which
 481 are the basis for the assessment of the adequacy of the uncertainty estimates, are shown
 482 in **Figs 8 (second row)**. The values generally are greater than 1.0, lying between
 483 1.5 and 3. Thus, uncertainty estimates may be too small by between 50% to 200%.
 484 However, some of these differences may not come from random errors because there
 485 are various degrees of differences between different pairs of methods. For example,
 486 $^{ell}\mathcal{I}_3^{DW}$ is systematically slower than \mathcal{I}_2^{AN} at shorter periods ($\langle \Delta \rangle \geq 0.5$ between 14 s and
 487 26 s, **Fig. 8a**), which may call into question the straight-ray correction and further
 488 improvements might require use of finite frequency sensitivity kernels. In addition,
 489 $\langle \Delta^2 \rangle$ generally increases with period, indicating the increasing finite frequency effects,

490 which are not considered in eikonal tomography (e.g. Lin and Ritzwoller, 2011b). Also,
 491 agreement between \mathcal{I}_2^{AN} and the three-station methods ($1.5 \leq \langle \Delta^2 \rangle \leq 2.5$, **Figs 8ac**)
 492 is slightly better than that between \mathcal{I}_2^{AN} and earthquake results ($2.5 \leq \langle \Delta^2 \rangle \leq 3$, **Fig.**
 493 **8e**), which is expected because three-station methods are based on and thus correlated
 494 with \mathcal{I}_2^{AN} (Sheng et al., 2018).

495 In summary, to produce $\langle \Delta^2 \rangle \sim 1$ requires the uncertainties $\sigma_{\bar{c}}$ to be upscaled by
 496 a factor of about 2 on average. Some of this upscaling will encompass the observed
 497 systematic biases between the maps. But, such biases are small enough for us to con-
 498 clude that for isotropic phase speed, measurements from the different methods can be
 499 combined consistently into a single data set (**section 5.1**).

500 4.3 Azimuthally anisotropic phase speed maps

501 4.3.1 Observation of apparent 1ψ anisotropy

502 Observations of apparent Rayleigh wave 1ψ azimuthal anisotropy (360° periodicity)
 503 have been reported in the western U.S. (Lin and Ritzwoller, 2011b) and Alaska (Feng
 504 et al., 2020), which are largely attributed to backward scattering from strong lateral
 505 isotropic velocity contrasts (Lin and Ritzwoller, 2011a). Because 1ψ anisotropy violates
 506 reciprocity and thus is non-physical, we attempt to detect it and to remove the bias
 507 it may cause in both isotropic and 2ψ anisotropic phase speed estimates (**Fig. 9**).
 508 In fact, by fitting local azimuth-dependent phase speeds with eq. (12), we do observe
 509 strong 1ψ anisotropy ($> 3\%$) at long periods (> 50 s), especially around the Cascade
 510 Range (**Figs 9ce**). The fast directions of 1ψ anisotropy, ψ_1 , mostly point towards the
 511 faster isotropic phase speed (**Figs 9df**), consistent with their being caused by backward
 512 scattering. Compared with fitting 2ψ anisotropy only, fitting 1ψ and 2ψ anisotropy si-
 513 multaneously makes a difference in 2ψ fast directions (MAD (median absolute deviation)
 514 of the difference $\sim 10^\circ$ (with respect to 0°)) and in isotropic phase speeds (MAD of the
 515 difference ~ 11 m/s).

516 4.3.2 Comparison of anisotropic maps from different methods

517 An example of 2ψ anisotropy (fast directions, ψ_2 , and amplitudes, A_2) with asso-
 518 ciated uncertainty estimates (σ_{ψ_2} and σ_{A_2}) constructed with the different methods is
 519 shown in **Fig. 10** at 30 s period. Qualitatively, the patterns of fast directions, ampli-
 520 tudes, and uncertainties between the methods are similar to one another, such as the two
 521 stripes of relatively strong anisotropy near the Cascade Range and at old lithospheric
 522 ages on the oceanic plate.

523 A quantitative comparison of the maps at 30 s period is presented in **Fig. 11**,
 524 which displays Δ_{ψ_2} and Δ_{A_2} between the method \mathcal{I}_2^{AN} and other methods. For fast
 525 directions ψ_2 , relatively large differences are principally observed where at least one
 526 of the methods yields low amplitudes, A_2 , or near the periphery of the maps where

527 azimuthal coverage for the noise-based methods is poor (**Figs 11aei**), such as the
 528 difference between \mathcal{I}_2^{AN} and earthquakes south of the Blanco Transform (**Fig. 11i**).
 529 Differences in A_2 appear to be more random although somewhat correlated with those
 530 in ψ_2 (**Figs 11cggk**). A notable exception is that A_2 near the northern Gorda Ridge
 531 from \mathcal{I}_2^{AN} is much stronger than that determined from earthquakes (**Fig. 11k**). Such
 532 large regional differences may provide constraints for uncertainty estimation.

533 Spatial statistics are summarized via histograms of the normalized differences for
 534 fast directions ψ_2 (**Figs 11bfj**) and amplitudes A_2 (**Figs 11dhl**). For instance, statistics
 535 for the comparison of A_2 between \mathcal{I}_2^{AN} and $^{ell}\mathcal{I}_3^{DW}$ are: $\langle\Delta_{A_2}\rangle = -0.4$, $\langle\Delta_{A_2}^2\rangle = 2.6$, and
 536 $\langle\epsilon_{A_2}\rangle = 0.30\%$ (**Fig. 11d**). That is, the spatial average of the normalized difference
 537 in anisotropy amplitude between the methods is -0.4 , which means that \mathcal{I}_2^{AN} produces
 538 lower anisotropy amplitudes at this period than $^{ell}\mathcal{I}_3^{DW}$ by about 40% of the average
 539 uncertainty, which is 0.30%. This is compatible with the criterion, $|\langle\Delta_{A_2}\rangle| \leq 1$, for the
 540 maps not to be considered systematically different. As indicated by $\langle\Delta_{A_2}^2\rangle = 2.6$, our
 541 uncertainties are probably underestimated for either or both of the methods. Other
 542 comparisons presented in **Fig. 11** are similar: systematic bias between the maps is
 543 below the threshold for indicating the maps to be systematically different while the
 544 uncertainties tend to be underestimated by about a factor of two.

545 Similar analyses are performed across all periods where results from the different
 546 methods overlap, and the statistics are plotted versus period for both anisotropy am-
 547 plitudes and fast directions in **Fig. 12**.

548 The assessment of systematic bias between different methods are shown in **Fig.**
 549 **12** for anisotropy amplitudes (**Fig. 12djpv**) and fast directions (**Fig. 12agms**). In
 550 general, the level of systematic bias between the methods is low ($|\langle\Delta\rangle| < 1$), except
 551 between \mathcal{I}_2^{AN} and EQ at periods of 36–40 s where amplitudes from EQ are smaller than
 552 \mathcal{I}_2^{AN} , which might be due to earthquake paths being much longer and thus having much
 553 larger sensitivity kernels. Thus, we conclude that the maps from the different methods
 554 are compatible, and the measurements derived from the methods can be combined.

555 The systematic bias can be converted from dimensionless to units if multiplied by
 556 the mean uncertainties. These uncertainties minimize around 24 s ($\langle\epsilon_{\psi_2}\rangle \sim 7^\circ$ and
 557 $\langle\epsilon_{A_2}\rangle \sim 0.25\%$) and increase at shorter and longer periods ($\langle\epsilon_{\psi_2}\rangle \sim 10^\circ$ and $\langle\epsilon_{A_2}\rangle \sim$
 558 0.5%). When multiplied by average uncertainties of $\langle\epsilon_{\psi_2}\rangle \sim 8^\circ$ and $\langle\epsilon_{A_2}\rangle \sim 0.3\%$, an
 559 average value of bias of ~ 0.5 corresponds to $\sim 4^\circ$ for ψ_2 and $\sim 0.15\%$ for A_2 , which are
 560 relatively low.

561 The underestimation of uncertainties for anisotropic parameters is comparable to
 562 that for isotropic phase speed. The standard deviations of the normalized differences,
 563 $\langle\Delta_{\psi_2}^2\rangle$ and $\langle\Delta_{A_2}^2\rangle$, are all greater than one, mostly between 1.5 and 2.5, for both ψ_2 (**Figs**
 564 **12bhnt**) and A_2 (**Figs 12flrx**). In addition, $\langle\Delta_{\psi_2}^2\rangle$ and $\langle\Delta_{A_2}^2\rangle$ also increase with period
 565 in general. These values are consistent with $\langle\Delta_{\bar{c}}^2\rangle$ (**Fig. 8**) and thus will be reduced
 566 to a similar level if uncertainties for azimuthally binned phase speed measurements are

567 appropriately upscaled before fitting (**section 4.1**).

568 In summary, to yield $\langle \Delta_{\psi_2}^2 \rangle$ and $\langle \Delta_{A_2}^2 \rangle$ about unity indicates that the uncertainties,
 569 σ_{ψ_2} and σ_{A_2} , need to be upscaled by a factor of ~ 2 , which is consistent with the extent
 570 of underestimation for isotropic phase speed uncertainties $\sigma_{\bar{c}}$ (**section 4.2**). Thus,
 571 an appropriate upscaling of uncertainties before fitting the azimuthally binned phase
 572 speeds (**section 4.1**) will reduce $\langle \Delta_{\bar{c}}^2 \rangle$, $\langle \Delta_{\psi_2}^2 \rangle$ and $\langle \Delta_{A_2}^2 \rangle$ all to a similar level (~ 1). This
 573 upscaling will also reduce the amplitude of the normalized systematic bias $|\langle \Delta \rangle|$ between
 574 the methods, so that an average bias about half the uncertainty level will be reduced
 575 to only a quarter of the upscaled uncertainty. Such small biases are compatible with
 576 the hypothesis that the methods are not systematically different, and thus we combine
 577 measurements from different methods to produce a single composite result (**section**
 578 **5.2**).

579 5 Composite results

580 To construct composite results, we combine the source-specific phase speed measure-
 581 ments across all methods (**Fig. 5**). Compared with combining the phase speed maps
 582 across methods (**Fig. 6**), combining the source-specific measurements before binning
 583 and stacking has the advantage of utilizing the complementary azimuthal coverages
 584 between the methods. Specifically, to construct a composite result with uncertainty
 585 at a given period and location, the source-specific phase speed measurements from all
 586 methods that exist at the location and period are combined by computing their mean
 587 and the SDOM for each azimuthal bin as observations (**Fig. 5e**). Then we fit eq. (12)
 588 to the binned statistics over azimuth to estimate the isotropic and anisotropic param-
 589 eters with associated uncertainties (**section 4.1**). We repeat this process at all locations
 590 across the region of study to produce the isotropic and anisotropic maps at the period.

591 5.1 Composite isotropic phase speed maps

592 In general, phase speeds on the oceanic plates are faster than the continental shelf
 593 and continents, and also vary less with period (**Fig. 13**). Near the continental shelf,
 594 phase speeds are relatively low, delineating the dichotomy between onshore and offshore
 595 structures. On the continents, phase speeds are more variable spatially and across
 596 different periods.

597 Previous studies have already constructed isotropic maps onshore (e.g. Lin et al.,
 598 2008; Shen and Ritzwoller, 2016), which are generally consistent with our results there.
 599 Less work has been done offshore, and our discussion of the composite maps here will
 600 focus on the offshore and near coastal regions for this reason (**Fig. 13**).

601 At 10 s period (**Figs 13ab**), the results derive from the two- and three-station
 602 ambient noise methods alone. Rayleigh wave phase speed at this period in the oceans
 603 is mostly sensitive to water depth, oceanic sediments, crustal thickness, and uppermost

604 mantle. On the continent, it is mostly sensitive to crustal structures. The phase speed
 605 at this period in the oceanic plate is much faster (> 3.6 km/s) than in the continent
 606 (~ 3.1 km/s). The Juan de Fuca Ridge, the Blanco Transform Fault, and the Gorda
 607 Ridge are delineated as relative slow anomalies offshore. A prominent slow stripe ($<$
 608 2.8 km/s) along the continental shelf (especially to the west of Washington) clearly
 609 separates the land from the ocean and may derive from the thick accretionary wedge
 610 (Horning et al., 2016). Uncertainties $\sigma_{\bar{c}}$ on the continents are quite small (~ 5 m/s),
 611 while the $\sigma_{\bar{c}}$ offshore is substantially larger (~ 10 m/s), especially on the continental
 612 shelf (~ 15 m/s).

613 At 20 s period (**Figs 13cd**), the results are also derived exclusively from the ambient
 614 noise methods. Rayleigh waves at this period are largely sensitive to the uppermost
 615 mantle offshore, and the middle and lower crust onshore with some sensitivity to the
 616 mantle in areas of relatively thin continental crust. The Cobb Hotspot near the Juan de
 617 Fuca Ridge stands out as a relatively slow anomaly in the ocean. The slow anomalies
 618 along the coast march landward compared to their location at 10 s period (**Fig. 13a**)
 619 and apparently break into two distinct zones in the northern and southern continental
 620 margin. Uncertainties $\sigma_{\bar{c}}$ are much smaller than at 10 s period (~ 3 m/s onshore and
 621 ~ 5 m/s offshore) because of the increase in SNR at 20 s period and the corresponding
 622 increase in the number of measurements (**section 3**).

623 At 30 s period (**Figs 13ef**), results are from both earthquakes and ambient noise.
 624 The Rayleigh wave at this period is largely sensitive to the uppermost mantle offshore,
 625 and the lower crust, crustal thickness, and uppermost mantle onshore. The slow ana-
 626 lies along the continental margin again break into northern and southern regions, but
 627 have lower amplitudes compared to shorter periods (**Figs 13ac**). Uncertainties $\sigma_{\bar{c}}$ are
 628 relatively homogeneous (~ 5 m/s) and are smaller than those from the individual data
 629 sets (**Fig. 6**) because of the increase of the number of measurements.

630 At 60 s period (**Figs 13gh**), the map is from earthquake data alone and Rayleigh
 631 wave dispersion is mainly sensitive to the upper mantle across the entire region. The two
 632 slow patches on the northern and southern continental margin are still clearly depicted
 633 but move oceanward again compared to 30 s period. Uncertainties $\sigma_{\bar{c}}$ have increased
 634 relative to 30 s period, both onshore (~ 7 m/s) and particularly offshore (~ 15 m/s).

635 5.2 Composite anisotropic maps

636 Generally, anisotropy amplitudes A_2 increase with lithospheric age on the oceanic
 637 plates and decrease with period (**Fig. 14**). A_2 is relatively weak ($< 2\%$) on the con-
 638 tinental shelf in general. On the continent, A_2 near the Cascade Range is relatively
 639 strong across most periods. In addition, fast directions ψ_2 are ridge-perpendicular at
 640 young ages and rotate counterclockwise with increasing age in general, although varia-
 641 tions exist between different periods and between the Juan de Fuca and Gorda Plates.
 642 Near the continental shelf, ψ_2 is more variable and shows both trench-perpendicular

643 and trench-parallel directions at different locations and periods. On the continent, ψ_2
 644 varies with location and period in a complex manner.

645 Because anisotropic structures onshore have been well studied and our results do
 646 not substantially differ from previous studies (e.g. Lin et al., 2011; Lin and Ritzwoller,
 647 2011b), the following discussion of the composite anisotropic maps focuses on the off-
 648 shore and near the coastal regions (**Fig. 14**).

649 At 12 s period (**Figs 14a-c**), maps are constructed from data using a combination
 650 of the ambient noise methods \mathcal{I}_2^{AN} , $ell\mathcal{I}_3^{DW}$ and $hyp\mathcal{I}_3^{DW}$. On the Juan de Fuca Plate, 2ψ
 651 fast directions ψ_2 rotate slightly counterclockwise from ridge-perpendicular to W-E as
 652 the plate ages, which is consistent with the paleo-spreading directions (calculated from
 653 gradients of lithospheric age (Wilson, 1993)). The anisotropy amplitudes A_2 generally
 654 increase with age. Near the Blanco Transform, fast axes ψ_2 run predominantly W-E,
 655 counterclockwise from the fault strike. On the Gorda Plate, fast axes rotate clockwise
 656 from ridge-perpendicular as the plate ages, aligning approximately with paleo-spreading
 657 directions, and A_2 is strong ($> 3\%$) except near the Gorda Ridge. On the northern
 658 continental shelf, fast axes run NNW-SSE and strong A_2 is observed. Relatively large
 659 uncertainties in ψ_2 are mainly due to small amplitudes, A_2 (**Fig. 14b**), while large
 660 uncertainties in A_2 are mostly on the continental shelf due to low data quality (**Fig.**
 661 **14c**).

662 At 30 s period (**Figs 14d-f**), the results combine ambient noise and earthquake data.
 663 On the Juan de Fuca Plate, fast axes ψ_2 are generally consistent with paleo-spreading
 664 directions except at the older ages (> 7 Ma) where they rotate counterclockwise from
 665 W-E towards WSW-ENE to align apparently with absolute plate motion directions. A
 666 high amplitude A_2 stripe is also observed at these older ages along the trench. On the
 667 Gorda Plate, fast axes are predominantly oriented W-E, apparently counterclockwise
 668 from paleo-spreading directions. On the continental shelf, fast axes show a substantial
 669 trench-parallel component and are substantially different from those on the oceanic
 670 plate as well as on the continent.

671 At 50 s period (**Figs 14g-i**), the results are from earthquake data alone. Near the
 672 Blanco Transform, fast axes ψ_2 align well with the strike of the fault, which is different
 673 from the shorter periods (**Figs 14a-f**) but similar to earthquake results at 30 s period
 674 (**Fig. 10j**). Along the trench on the oceanic plates, the strong A_2 stripe appears to
 675 diminish, which could be due to the use of earthquake data alone at this period (**Fig.**
 676 **12p**) or the structure itself (Eilon and Forsyth, 2020). On the continental shelf, fast
 677 axes are predominantly trench-perpendicular while the amplitudes A_2 are relatively
 678 weak ($< 1\%$).

679 At 80 s period (**Figs 14j-l**), results also are only from earthquake data. Near the
 680 Blanco Transform, strong amplitudes A_2 are observed and fast axes ψ_2 are parallel to
 681 the fault strike. On the Juan de Fuca Plate, the strong A_2 stripe along the trench
 682 apparent at shorter periods has disappeared. On the Gorda Plate, fast axes rotate
 683 counterclockwise from ridge-perpendicular to W-E as the plate ages, and amplitudes

684 A_2 are strong ($> 3\%$) except near the Gorda Ridge.

685 Crustal and mantle anisotropy near a target location is reflected in anisotropic dis-
686 persion curves, which are constructed by extracting the anisotropic parameters A_2 and
687 ψ_2 from the period-dependent maps (e.g. Lin et al., 2011). The period-dependent pat-
688 terns of fast axes and amplitudes differ appreciably at different locations, as **Fig. 15**
689 shows for four locations. At a point near the Juan de Fuca Ridge, a change in fast axis
690 ψ_2 from ridge-perpendicular (NW-SE) to nearly N-S corresponds to the minimum of am-
691 plitude A_2 (**Figs 15ab**), suggesting a change of anisotropy at deeper depth. For a point
692 within the Juan de Fuca Plate, ψ_2 is mostly W-E while A_2 slightly increases then de-
693 creases with period (**Figs 15cd**), suggesting vertically relatively coherent deformation.
694 At a point on the continental shelf, ψ_2 is predominantly trench parallel (NE-SW) and A_2
695 varies slowly with period (**Figs 15ef**), indicating complicated changes in anisotropy be-
696 tween the sediments and crust. For a point in Oregon, both ψ_2 and A_2 apparently break
697 into three segments with ψ_2 rotating counterclockwise from N-S to W-E then to NE-SW
698 and A_2 increasing then decreasing with period (**Figs 15gh**), indicating distinctions be-
699 tween upper crust, lower crust, and mantle. Such anisotropic dispersion curves can serve
700 as the basis for 3-D azimuthally anisotropic model inversions (**FengRitzwoller_2020**;
701 e.g. Lin et al., 2011). When information about radial anisotropy is available from Love
702 wave dispersion (e.g. Moschetti et al., 2010; Feng and Ritzwoller, 2019), azimuthally
703 and radially anisotropic dispersion curves can be combined to constrain a tilted depth-
704 dependent hexagonally symmetric medium for simultaneous explanation of azimuthal
705 and radial anisotropy (e.g. Xie et al., 2015; Xie et al., 2017). Anisotropy from surface
706 waves can also complement body wave observations, such as shear wave splitting (e.g.
707 Martin-Short et al., 2015; Bodmer et al., 2015) and P_n waves (e.g. VanderBeek and
708 Toomey, 2017; VanderBeek and Toomey, 2019), to achieve a better depth resolution
709 (e.g. Lin et al., 2011; Eilon and Forsyth, 2020).

710 6 Discussion

711 6.1 Comparison with previous studies

712 6.1.1 Isotropic structures

713 Janiszewski et al. (2019) constructed Rayleigh wave isotropic phase speed maps
714 from two-station ambient noise interferometry (\mathcal{I}_2^{AN}) and earthquake tomography. We
715 compare both our local dispersion curves and phase speed maps with theirs and find
716 significant discrepancies. We do not completely understand the cause of the discrepan-
717 cies, but an appreciable part probably results from differences in methodology between
718 our study and theirs.

719 Dispersion curves at a location extracted from the phase speed maps at different
720 periods should be reasonably smooth to make physical sense. For visual comparison,

721 **Fig. 16** presents dispersion curves at several locations from our different methods and
 722 from Janiszewski et al. (2019). The dispersion curves from our methods are presented
 723 as corridors with a thickness defined by our uncertainties at the location: $\bar{c} \pm 2\sigma_{\bar{c}}$. Our
 724 results nearly overlap each other, which illustrates the consistency that emerges from our
 725 different methods. The fact that Janiszewski et al. (2019) also estimated uncertainties
 726 allows us to present their results at the same locations similarly. We find, however, that
 727 significant discrepancies ($> 5\%$) appear between our results and those of Janiszewski
 728 et al. (2019), even on the continent (**Fig. 16d**).

729 A more detailed comparison of our phase speed maps with those from Janiszewski
 730 et al. (2019) is presented here in terms of maps and histograms of raw differences.
 731 We do not use normalized differences as in **section 4.1**, because their approach to
 732 uncertainty estimates is different from ours. We present comparisons at each period in
 733 the supplementary material (**Figs S3-S10**). The spatial mean of the raw differences
 734 and the combined uncertainties are summarized in **Fig. 17**.

735 Our maps are systematically faster than their ambient noise maps, and the bias
 736 increases with period from ~ 15 m/s at 10 s to ~ 60 m/s at 20 s, which corresponds
 737 to $\sim 0.5\%$ and $\sim 2\%$ for a phase speed of 3 km/s, respectively. This discrepancy may
 738 be due to the fact that they did not denoise the OBS data with tilt and compliance
 739 noise corrections (their two-station interferograms are from Gao and Shen (2015)). In
 740 contrast, our maps are systematically slower than their earthquake maps, and the bias
 741 also increases with period but with an opposite sign from -20 m/s at 20 s to -40 m/s at
 742 80 s ($\sim 1\%$ for a phase speed of 3 km/s), which might be due to different implementations
 743 of Helmholtz tomography (Jin and Gaherty, 2015). The largest bias is between their
 744 ambient noise and earthquake results (earthquake results ~ 70 m/s faster), which they
 745 attribute partly to the difference in station distribution.

746 6.1.2 Azimuthally anisotropic structures

747 A quantitative comparison requires a 3-D model inversion, which we do not produce
 748 here. Here we only provide a qualitative comparison of azimuthally anisotropic struc-
 749 tures with those observed from earthquake P_n waves, Rayleigh waves, and shear wave
 750 splitting.

751 At 12 s period (**Figs 14a-c**), the Rayleigh wave is mainly sensitive to the oceanic
 752 uppermost mantle, so azimuthal anisotropy from Rayleigh waves is comparable to that
 753 from P_n waves. Indeed, the following patterns in our results are also observed in 2ψ fast
 754 directions from P_n (VanderBeek and Toomey, 2017; VanderBeek and Toomey, 2019):
 755 ridge-perpendicular near the Juan de Fuca Ridge, W-E on the Juan de Fuca Plate
 756 interior and near the Blanco Transform, and clockwise rotation with age on the Gorda
 757 Plate.

758 Eilon and Forsyth (2020) use earthquake surface waves (measurements from Bell
 759 et al., 2016; Ruan et al., 2018) to infer azimuthal anisotropy in four subregions: Juan

760 de Fuca Plate, Gorda Plate, Blanco Transform, and Juan de Fuca Ridge (Bodmer et
761 al., 2015), with homogeneous anisotropic parameters in each subregion. An apparent
762 discrepancy between our results and theirs is that they find the fast directions ψ_2 on the
763 Juan de Fuca Plate to be WSW-ENE at periods < 80 s while we observe substantial W-
764 E directions (e.g. **Figs 14dg**). In addition to methodological differences (e.g. they used
765 the two-plane wave tomography), the discrepancy might partly arise from the difference
766 in presenting the results. For instance, as the plate ages at 30 s period (**Fig. 14d**),
767 we find ψ_2 to rotate from W-E to WSW-ENE and A_2 to increase, so that the regional
768 result will be predominantly WSW-ENE if measurements at each individual location
769 are weighed by A_2 .

770 At long periods (**Figs 14gj**), we find remarkable consistency with *SKS* splitting
771 results (Bodmer et al., 2015; Martin-Short et al., 2015) that ψ_2 rotates counterclockwise
772 from fault parallel at the Blanco Transform (NW-SE) to ridge perpendicular on the
773 Gorda Plate (WNW-ESE) to WSW-ENE at Oregon and northern California. However,
774 on the Juan de Fuca Plate, A_2 from *SKS* does not vary significantly with age, and
775 ψ_2 is mostly WSW-ENE, indicating increased A_2 at young ages and ψ_2 being mostly
776 WSW-ENE at deeper depths.

777 6.2 Enigmatic features

778 Here we point out several enigmatic anisotropic structures that await further inves-
779 tigation.

780 At 12 s period (**Fig. 14a**), there are two strong anisotropy regions in the northern
781 Juan de Fuca Plate and continental shelf in which the fast directions are almost per-
782 pendicular to one another. Long paths crossing both regions would average out and
783 might cause such artifacts in traditional path-based tomography methods. However, the
784 eikonal tomography approach used here utilizes the local wavefield gradient and thus
785 is not prone to misinterpretation caused by long paths. We also try to identify prob-
786 lematic stations (see supplementary material), but removing them only slightly reduces
787 the amplitudes and does not change the fast directions substantially. Because the OBS
788 are noisier in shallow waters, structures on the continental shelf are relatively less well
789 resolved from eikonal tomography. Traditional path-based tomography methods might
790 complement eikonal tomography there using paths between deep water OBS and land
791 stations.

792 At 30 s period (**Fig. 14d**), two nearly parallel bands of large amplitudes, one near
793 the trench and the other along the coast, are similar in width, A_2 , and ψ_2 . Because
794 they are roughly equidistant from the continental shelf with ψ_2 mostly W-E, one may
795 wonder if this is caused by localized noise sources. Indeed, Tian and Ritzwoller (2015)
796 find that the primary microseism sources originate significantly from shallow waters
797 along the coast. Because eikonal tomography derives directly from the wave equation
798 and holds for any source, however, it should still work for one-sided sources (Lin et al.,

799 2009). Another hypothesis is refraction or reflection of phases at the transition (personal
800 communication with Donald Forsyth).

801 7 Conclusion

802 Our final product is a set of composite Rayleigh wave isotropic and azimuthally
803 anisotropic phase speed maps from 10 s to 80 s period, constructed by combining earth-
804 quake (28–80 s) and ambient noise-based (10–40 s) data. Compared with two-station
805 interferometry (\mathcal{I}_2^{AN}), three-station direct-wave interferometry methods ($^{ell}\mathcal{I}_3^{DW}$ and
806 $^{hyp}\mathcal{I}_3^{DW}$) provide $> 50\%$ enhancement in the SNR and the number of dispersion mea-
807 surements which is particularly noteworthy in the noisier oceanic environment (**section**
808 **3**). This illustrates the potential utility of the method in other amphibious settings
809 such as off Alaska using data from AACSE (Alaska Amphibious Community Seismic
810 Experiment, (Abers and Wiens, 2018)). The isotropic (**section 4.2**) and azimuthally
811 anisotropic (**section 4.3**) phase speed maps based on earthquakes and ambient noise
812 data agree within about twice the estimated uncertainties. This reflects positively on
813 the effectiveness of denoising of OBS data (**section 2.1.1**) and on de-biasing the three-
814 station methods (**section 2.1.2**). Compared with maps from each method alone, the
815 composite maps reduce uncertainties, broaden the bandwidth, and improve azimuthal
816 coverage (**section 5**).

817 The composite isotropic phase speed maps have a resolution $\sim 0.6^\circ$ with mean frac-
818 tional uncertainties of 0.1–0.3% onshore (4–8 m/s) and 0.15–0.5% offshore (5–20 m/s).
819 Uncertainties minimize between 20 s and 40 s period and increase at shorter and longer
820 periods. Isotropic anomalies (**section 5.1**) qualitatively correlate with known geologi-
821 cal features, such as the Juan de Fuca and Gorda Ridges, the Cobb hotspot, the Blanco
822 Transform Fault, and the Cascade Range.

823 The composite azimuthally anisotropic phase speed maps have a resolution of $\sim 1.2^\circ$
824 with mean fractional uncertainties of 1–5% onshore ($2\text{--}10^\circ$) and 2–6% offshore ($3\text{--}12^\circ$)
825 for fast direction, ψ_2 , and 6–30% onshore (0.1–0.2%) and 11–40% offshore (0.15–0.5%)
826 for amplitude, A_2 . Uncertainties vary with period similarly to those of isotropic maps
827 (**section 4.3**). On the oceanic plate, the 2ψ fast directions qualitatively align with
828 paleo-spreading directions while the 2ψ amplitudes generally increase with lithospheric
829 age, both showing nontrivial variations with period (**section 5.2**). Strong ($> 3\%$)
830 apparent 1ψ azimuthal anisotropy is observed at long periods (> 50 s) around the Cas-
831 cade Range, probably caused by backward scattering from strong isotropic heterogeneity
832 (**section 4.3.1**).

833 Our comparisons between different methods provide important constraints on un-
834 certainty estimates. First, the spatial statistics of the differences between the methods
835 indicate that on average we underestimate uncertainties by 50–150% for both isotropic
836 and anisotropic structures, probably because systematic errors are not accounted for

837 (Lin et al., 2009). Second, nonrandom and significant differences at some periods and
838 regions awaits further investigation (e.g. the differences at 30 s near the Cascade Range
839 between earthquake- and noise-based maps in **Fig. 7e**). These caveats call for attention
840 in future usage of the uncertainties and interpretation of the structures.

841 The composite phase speed maps are designed to serve as a basis for future work.
842 One possible extension is to invert for 3-D shear velocity models based on the maps,
843 potentially jointly with other observables such as receiver functions (e.g. Janiszewski
844 and Abers, 2015; Audet, 2016; Rychert et al., 2018), Rayleigh wave ellipticity, and
845 Rayleigh wave displacement to pressure ratios (e.g. Ruan et al., 2014). Different from
846 traditional seismic parameterizations, thermal parameterizations (e.g. Shapiro and Ritz-
847 woller, 2004) may be used as hypothesis tests on the thermal state of the oceanic litho-
848 sphere (e.g. Tian et al., 2013). Surface wave azimuthal anisotropy observations can
849 complement body wave data such as shear wave splitting (e.g. Martin-Short et al.,
850 2015; Bodmer et al., 2015) for 3-D anisotropic model inversions (e.g. Lin et al., 2011).
851 Observations of Love waves can be combined with Rayleigh waves to constrain a tilted
852 hexagonally symmetric medium for simultaneous explanation of azimuthal and radial
853 anisotropy (e.g. Xie et al., 2015). Such anisotropic models may provide constraints for
854 geodynamical simulations of deformation across and beneath the lithosphere.

855 Acknowledgement

856 We thank the editor, Michal Malinowski, and the reviewers, Donald Forsyth and
857 anonymous, for constructive comments. We appreciate the generosity from Helen
858 Janiszewski for providing phase speed maps (Janiszewski et al., 2019) to compare with
859 our own and from Weisen Shen for sharing onshore ambient noise correlations and earth-
860 quake dispersion measurements from the TA (Shen and Ritzwoller, 2016). The authors
861 are grateful to the Cascadia Initiative Expedition Team for acquiring the Amphibi-
862 ous Array Ocean Bottom Seismograph data and appreciate the open data policy that
863 makes these data available. This work utilized resources from the University of Colorado
864 Boulder Research Computing Group, which is supported by the National Science Foun-
865 dation (awards ACI-1532235 and ACI-1532236), the University of Colorado Boulder,
866 and Colorado State University. **Author contributions:** S.Z. computed three-station
867 interferograms, applied tomography analysis, and co-wrote the paper. H.W. prepro-
868 cessed noise data and computed two-station interferograms. M.W. preprocessed and
869 measured dispersion from earthquake data. M.H.R. designed and guided the project
870 and co-wrote the paper. All authors discussed the results and provided comments on
871 the manuscript. **Funding:** Aspects of this research were supported in part by NSF
872 grants EAR-1537868, EAR-1645269, and EAR-1928395 at the University of Colorado
873 at Boulder. **Data and materials availability:** Our composite phase speed maps
874 are available on Zenodo (doi: [10.5281/zenodo.3973769](https://doi.org/10.5281/zenodo.3973769)). Source codes for this project

875 are available on GitHub (<https://github.com/NoiseCIEI>) or upon request from the
876 corresponding author. The offshore data used in this research were provided by instru-
877 ments from the Ocean Bottom Seismograph Instrument Pool (<http://www.obsip.org>)
878 which is funded by the National Science Foundation. OBSIP data are archived at the
879 IRIS Data Management Center (<http://www.iris.edu>). The facilities of IRIS Data
880 Services, and specifically the IRIS Data Management Center, were used for access to
881 waveforms, related metadata, and/or derived products used in this study. IRIS Data
882 Services are funded through the Seismological Facilities for the Advancement of Geo-
883 science and EarthScope (SAGE) Proposal of the National Science Foundation under
884 Cooperative Agreement EAR-1261681.

885 **References**

- 886 Abers, G. and D. Wiens (2018). “AACSE: Alaska Amphibious Community Seismic
887 Experiment”. International Federation of Digital Seismograph Networks. DOI: [10.7914/SN/X0_2018](https://doi.org/10.7914/SN/X0_2018).
888
- 889 Atwater, B. F. (1987). “Evidence for great Holocene earthquakes along the outer coast
890 of Washington State”. *Science* 236.4804, pp. 942–944. DOI: [10.1126/science.236.4804.942](https://doi.org/10.1126/science.236.4804.942).
891
- 892 Audet, P. (2016). “Receiver functions using OBS data: promises and limitations from
893 numerical modelling and examples from the Cascadia Initiative”. *Geophysical journal
894 international* 205.3, pp. 1740–1755. DOI: [10.1093/gji/ggw111](https://doi.org/10.1093/gji/ggw111).
- 895 Barmin, M. P., M. H. Ritzwoller, and A. L. Levshin (2001). “A fast and reliable method
896 for surface wave tomography”. *Pure and applied geophysics* 158.8, pp. 1351–1375.
897 DOI: [10.1007/978-3-0348-8264-4_3](https://doi.org/10.1007/978-3-0348-8264-4_3).
- 898 Bell, S., D. W. Forsyth, and Y. Ruan (2015). “Removing noise from the vertical compo-
899 nent records of ocean-bottom seismometers: results from year one of the Cascadia
900 Initiative”. *Bulletin of the seismological society of america* 105.1, pp. 300–313. DOI:
901 [10.1785/0120140054](https://doi.org/10.1785/0120140054).
- 902 Bell, S., Y. Ruan, and D. W. Forsyth (2016). “Ridge asymmetry and deep aqueous
903 alteration at the trench observed from Rayleigh wave tomography of the Juan de
904 Fuca plate”. *Journal of geophysical research: solid earth* 121.10, pp. 7298–7321. DOI:
905 [10.1002/2016JB012990](https://doi.org/10.1002/2016JB012990).
- 906 Bensen, G. D., M. H. Ritzwoller, M. P. Barmin, A. L. Levshin, F. Lin, M. P. Moschetti,
907 N. M. Shapiro, and Y. Yang (2007). “Processing seismic ambient noise data to ob-
908 tain reliable broad-band surface wave dispersion measurements”. *Geophysical journal
909 international* 169.3, pp. 1239–1260. DOI: [10.1111/j.1365-246X.2007.03374.x](https://doi.org/10.1111/j.1365-246X.2007.03374.x).
- 910 Bird, P. (2003). “An updated digital model of plate boundaries”. *Geochemistry, geo-
911 physics, geosystems* 4.3. DOI: [10.1029/2001GC000252](https://doi.org/10.1029/2001GC000252).
- 912 Bodmer, M., D. R. Toomey, E. E. Hooft, J. Nábělek, and J. Braunmiller (2015). “Seis-
913 mic anisotropy beneath the Juan de Fuca plate system: Evidence for heterogeneous
914 mantle flow”. *Geology* 43.12, pp. 1095–1098. DOI: [10.1130/G37181.1](https://doi.org/10.1130/G37181.1).
- 915 Bodmer, M., D. R. Toomey, E. E. Hooft, and B. Schmandt (2018). “Buoyant astheno-
916 sphere beneath Cascadia influences megathrust segmentation”. *Geophysical research
917 letters* 45.14, pp. 6954–6962. DOI: [10.1029/2018GL078700](https://doi.org/10.1029/2018GL078700).
- 918 Byrnes, J. S., D. R. Toomey, E. E. Hooft, J. Nábělek, and J. Braunmiller (2017).
919 “Mantle dynamics beneath the discrete and diffuse plate boundaries of the Juan de
920 Fuca plate: results from Cascadia Initiative body wave tomography”. *Geochemistry,
921 geophysics, geosystems* 18.8, pp. 2906–2929. DOI: [10.1002/2017GC006980](https://doi.org/10.1002/2017GC006980).
- 922 Campillo, M. and A. Paul (2003). “Long-range correlations in the diffuse seismic coda”.
923 *Science* 299.5606, pp. 547–549. DOI: [10.1126/science.1078551](https://doi.org/10.1126/science.1078551).

- 924 Chen, Y. and E. Saygin (2020). “Empirical Green’s function retrieval using ambient
925 noise source-receiver interferometry”. *Journal of geophysical research: solid earth*
926 125.2, e2019JB018261. DOI: [10.1029/2019JB018261](https://doi.org/10.1029/2019JB018261).
- 927 Crawford, W. C. and S. C. Webb (2000). “Identifying and removing tilt noise from low-
928 frequency (< 0.1 Hz) seafloor vertical seismic data”. *Bulletin of the seismological*
929 *society of america* 90.4, pp. 952–963.
- 930 Curtis, A., Y. Behr, E. Entwistle, E. Galetti, J. Townend, and S. Bannister (2012).
931 “The benefit of hindsight in observational science: Retrospective seismological ob-
932 servations”. *Earth and planetary science letters* 345-348, pp. 212–220. DOI: [10.1016/
933 j.epsl.2012.06.008](https://doi.org/10.1016/j.epsl.2012.06.008).
- 934 Curtis, A. and D. Halliday (2010). “Source-receiver wave field interferometry”. *Physical*
935 *review e* 81.4, p. 046601. DOI: [10.1103/PhysRevE.81.046601](https://doi.org/10.1103/PhysRevE.81.046601).
- 936 Dziewonski, A., S. Bloch, and M. Landisman (1969). “A technique for the analysis
937 of transient seismic signals”. *Bulletin of the seismological society of america* 59.1,
938 pp. 427–444.
- 939 Eilon, Z. C. and G. A. Abers (2017). “High seismic attenuation at a mid-ocean ridge
940 reveals the distribution of deep melt”. *Science advances* 3.5, e1602829. DOI: [10.
941 1126/sciadv.1602829](https://doi.org/10.1126/sciadv.1602829).
- 942 Eilon, Z. C. and D. W. Forsyth (2020). “Depth dependent azimuthal anisotropy beneath
943 the Juan de Fuca Plate system”. *Journal of geophysical research: solid earth* n/a.n/a,
944 e2020JB019477. DOI: [10.1029/2020JB019477](https://doi.org/10.1029/2020JB019477).
- 945 Feng, L., C. Liu, and M. H. Ritzwoller (2020). “Azimuthal anisotropy of the crust
946 and uppermost mantle beneath Alaska”. *Journal of geophysical research: solid earth*
947 125.12, e2020JB020076. DOI: [10.1029/2020JB020076](https://doi.org/10.1029/2020JB020076).
- 948 Feng, L. and M. H. Ritzwoller (2019). “A 3-D shear velocity model of the crust and
949 uppermost mantle beneath alaska including apparent radial anisotropy”. *Journal of*
950 *geophysical research: solid earth* 124.10, pp. 10468–10497. DOI: [10.1029/2019JB018122](https://doi.org/10.1029/2019JB018122).
- 951 Fenneman, N. M. and D. W. Johnson (1946). *Physical divisions of the United States*.
952 Reston, VA: US Geological Survey.
- 953 Gao, H. (2016). “Seismic velocity structure of the Juan de Fuca and Gorda Plates
954 revealed by a joint inversion of ambient noise and regional earthquakes”. *Geophysical*
955 *research letters* 43.10, pp. 5194–5201. DOI: [10.1002/2016GL069381](https://doi.org/10.1002/2016GL069381).
- 956 Gao, H. and Y. Shen (2015). “A preliminary full-wave ambient-noise tomography model
957 spanning from the Juan de Fuca and Gorda spreading centers to the Cascadia
958 volcanic arc”. *Seismological research letters* 86.5, pp. 1253–1260. DOI: [10.1785/
959 0220150103](https://doi.org/10.1785/0220150103).
- 960 GEBCO Compilation Group (2019). “GEBCO 2019 grid”. DOI: [10.5285/836f016a-
961 33be-6ddc-e053-6c86abc0788e](https://doi.org/10.5285/836f016a-33be-6ddc-e053-6c86abc0788e).
- 962 Goldfinger, C., C. H. Nelson, A. E. Morey, J. E. Johnson, J. R. Patton, E. B. Kara-
963 banov, J. Gutierrez-Pastor, A. T. Eriksson, E. Gracia, G. Dunhill, R. J. Enkin, A.
964 Dallimore, and T. Vallier (2012). *Turbidite event history—Methods and implications*

- 965 for Holocene paleoseismicity of the Cascadia subduction zone. USGS Numbered Se-
966 ries 1661-F. Reston, VA: U.S. Geological Survey. DOI: [10.3133/pp1661F](https://doi.org/10.3133/pp1661F).
- 967 Hawley, W. B. and R. M. Allen (2019). “The Fragmented Death of the Farallon Plate”.
968 *Geophysical research letters* 46.13, pp. 7386–7394. DOI: [10.1029/2019GL083437](https://doi.org/10.1029/2019GL083437).
- 969 Hawley, W. B., R. M. Allen, and M. A. Richards (2016). “Tomography reveals buoyant
970 asthenosphere accumulating beneath the Juan de Fuca Plate”. *Science* 353.6306,
971 pp. 1406–1408. DOI: [10.1126/science.aad8104](https://doi.org/10.1126/science.aad8104).
- 972 Horning, G., J. P. Canales, S. M. Carbotte, S. Han, H. Carton, M. R. Nedimović, and
973 P. E. van Keken (2016). “A 2-D tomographic model of the Juan de Fuca plate from
974 accretion at axial seamount to subduction at the Cascadia margin from an active
975 source ocean bottom seismometer survey”. *Journal of geophysical research: solid
976 earth* 121.8, pp. 5859–5879. DOI: [10.1002/2016JB013228](https://doi.org/10.1002/2016JB013228).
- 977 Hyndman, R. D. and K. Wang (1993). “Thermal constraints on the zone of major thrust
978 earthquake failure: the Cascadia subduction zone”. *Journal of geophysical research:
979 solid earth* 98.B2, pp. 2039–2060. DOI: [10.1029/92JB02279](https://doi.org/10.1029/92JB02279).
- 980 Janiszewski, H. A. and G. A. Abers (2015). “Imaging the plate interface in the Cascadia
981 seismogenic zone: new constraints from offshore receiver functions”. *Seismological
982 research letters* 86.5, pp. 1261–1269. DOI: [10.1785/0220150104](https://doi.org/10.1785/0220150104).
- 983 Janiszewski, H. A., J. B. Gaherty, G. A. Abers, H. Gao, and Z. C. Eilon (2019).
984 “Amphibious surface-wave phase-velocity measurements of the Cascadia subduc-
985 tion zone”. *Geophysical journal international* 217.3, pp. 1929–1948. DOI: [10.1093/
986 gji/ggz051](https://doi.org/10.1093/gji/ggz051).
- 987 Jin, G. and J. B. Gaherty (2015). “Surface wave phase-velocity tomography based on
988 multichannel cross-correlation”. *Geophysical journal international* 201.3, pp. 1383–
989 1398. DOI: [10.1093/gji/ggv079](https://doi.org/10.1093/gji/ggv079).
- 990 Kästle, E. D., R. Soomro, C. Weemstra, L. Boschi, and T. Meier (2016). “Two-receiver
991 measurements of phase velocity: cross-validation of ambient-noise and earthquake-
992 based observations”. *Geophysical journal international* 207.3, pp. 1493–1512. DOI:
993 [10.1093/gji/ggw341](https://doi.org/10.1093/gji/ggw341).
- 994 Levshin, A. L. and M. H. Ritzwoller (2001). “Automated detection, extraction, and
995 measurement of regional surface waves”. *Pure and applied geophysics* 158.8, pp. 1531–
996 1545. DOI: [10.1007/978-3-0348-8264-4_11](https://doi.org/10.1007/978-3-0348-8264-4_11).
- 997 Lin, F.-C., M. P. Moschetti, and M. H. Ritzwoller (2008). “Surface wave tomography
998 of the western United States from ambient seismic noise: Rayleigh and Love wave
999 phase velocity maps”. *Geophysical journal international* 173.1, pp. 281–298. DOI:
1000 [10.1111/j.1365-246X.2008.03720.x](https://doi.org/10.1111/j.1365-246X.2008.03720.x).
- 1001 Lin, F.-C. and M. H. Ritzwoller (2011a). “Apparent anisotropy in inhomogeneous isotropic
1002 media”. *Geophysical journal international* 186.3, pp. 1205–1219. DOI: [10.1111/j.
1003 1365-246X.2011.05100.x](https://doi.org/10.1111/j.1365-246X.2011.05100.x).

- 1004 Lin, F.-C. and M. H. Ritzwoller (2011b). “Helmholtz surface wave tomography for
1005 isotropic and azimuthally anisotropic structure”. *Geophysical journal international*
1006 186.3, pp. 1104–1120. DOI: [10.1111/j.1365-246X.2011.05070.x](https://doi.org/10.1111/j.1365-246X.2011.05070.x).
- 1007 Lin, F.-C., M. H. Ritzwoller, and R. Snieder (2009). “Eikonal tomography: surface wave
1008 tomography by phase front tracking across a regional broad-band seismic array”.
1009 *Geophysical journal international* 177.3, pp. 1091–1110. DOI: [10.1111/j.1365-
1010 246X.2009.04105.x](https://doi.org/10.1111/j.1365-246X.2009.04105.x).
- 1011 Lin, F.-C., M. H. Ritzwoller, Y. Yang, M. P. Moschetti, and M. J. Fouch (2011). “Com-
1012 plex and variable crustal and uppermost mantle seismic anisotropy in the western
1013 United States”. *Nature geoscience* 4.1, pp. 55–61. DOI: [10.1038/ngeo1036](https://doi.org/10.1038/ngeo1036).
- 1014 Lin, F.-C., V. C. Tsai, and M. H. Ritzwoller (2012). “The local amplification of sur-
1015 face waves: a new observable to constrain elastic velocities, density, and anelastic
1016 attenuation”. *Journal of geophysical research: solid earth* 117.B6. DOI: [10.1029/
1017 2012JB009208](https://doi.org/10.1029/2012JB009208).
- 1018 Liu, X. (2020). “Finite-frequency sensitivity kernels for seismic noise interferometry
1019 based on differential time measurements”. *Journal of geophysical research: solid earth*
1020 125.4, e2019JB018932. DOI: [10.1029/2019JB018932](https://doi.org/10.1029/2019JB018932).
- 1021 Ma, S. and G. C. Beroza (2012). “Ambient-field Green’s functions from asynchronous
1022 seismic observations”. *Geophysical research letters* 39.6, p. L06301. DOI: [10.1029/
1023 2011GL050755](https://doi.org/10.1029/2011GL050755).
- 1024 Martin-Short, R., R. M. Allen, I. D. Bastow, E. Totten, and M. A. Richards (2015).
1025 “Mantle flow geometry from ridge to trench beneath the Gorda–Juan de Fuca plate
1026 system”. *Nature geoscience* 8.12, pp. 965–968. DOI: [10.1038/ngeo2569](https://doi.org/10.1038/ngeo2569).
- 1027 Moschetti, M. P., M. H. Ritzwoller, F.-C. Lin, and Y. Yang (2010). “Crustal shear
1028 wave velocity structure of the western United States inferred from ambient seismic
1029 noise and earthquake data”. *Journal of geophysical research* 115.B10. DOI: [10.1029/
1030 2010JB007448](https://doi.org/10.1029/2010JB007448).
- 1031 Nabelek, J. and J. Braunmiller (2012). “Plate boundary evolution and physics at an
1032 oceanic transform fault system”. International Federation of Digital Seismograph
1033 Networks. Dataset/Seismic Network. DOI: [10.7914/SN/X9_2012](https://doi.org/10.7914/SN/X9_2012).
- 1034 — (2013). “Seismicity, structure and dynamics of the Gorda deformation zone.” In-
1035 ternational Federation of Digital Seismograph Networks. Dataset/Seismic Network.
1036 DOI: [10.7914/SN/Z5_2013](https://doi.org/10.7914/SN/Z5_2013).
- 1037 Nelson, A. R., B. F. Atwater, P. T. Bobrowsky, L.-A. Bradley, J. J. Clague, G. A. Carver,
1038 M. E. Darienzo, W. C. Grant, H. W. Krueger, R. Sparks, T. W. Stafford, and M.
1039 Stuiver (1995). “Radiocarbon evidence for extensive plate-boundary rupture about
1040 300 years ago at the Cascadia subduction zone”. *Nature* 378.6555, pp. 371–374. DOI:
1041 [10.1038/378371a0](https://doi.org/10.1038/378371a0).
- 1042 Ritzwoller, M. H. and L. Feng (2019). “Overview of pre- and post-processing of ambient-
1043 noise correlations”. *Seismic ambient noise*. Ed. by N. Nakata, L. Gualtieri, and A.
1044 Fichtner. Cambridge: Cambridge University Press. DOI: [10.1017/9781108264808](https://doi.org/10.1017/9781108264808).

- 1045 Ruan, Y., D. W. Forsyth, and S. W. Bell (2014). “Marine sediment shear velocity
1046 structure from the ratio of displacement to pressure of Rayleigh waves at seafloor”.
1047 *Journal of geophysical research: solid earth* 119.8, pp. 6357–6371.
- 1048 — (2018). “Shear attenuation beneath the Juan de Fuca plate: Implications for mantle
1049 flow and dehydration”. *Earth and planetary science letters* 496, pp. 189–197. DOI:
1050 [10.1016/j.epsl.2018.05.035](https://doi.org/10.1016/j.epsl.2018.05.035).
- 1051 Rychert, C. A., N. Harmon, and S. Tharimena (2018). “Scattered wave imaging of the
1052 oceanic plate in Cascadia”. *Science advances* 4.2, eaao1908. DOI: [10.1126/sciadv.
1053 aao1908](https://doi.org/10.1126/sciadv.aao1908).
- 1054 Sabra, K. G., P. Gerstoft, P. Roux, W. A. Kuperman, and M. C. Fehler (2005). “Surface
1055 wave tomography from microseisms in Southern California”. *Geophysical research
1056 letters* 32.14, p. L14311. DOI: [10.1029/2005GL023155](https://doi.org/10.1029/2005GL023155).
- 1057 Satake, K., K. Shimazaki, Y. Tsuji, and K. Ueda (1996). “Time and size of a giant
1058 earthquake in Cascadia inferred from Japanese tsunami records of January 1700”.
1059 *Nature* 379.6562 (6562), pp. 246–249. DOI: [10.1038/379246a0](https://doi.org/10.1038/379246a0).
- 1060 Shapiro, N. M. and M. Campillo (2004). “Emergence of broadband Rayleigh waves
1061 from correlations of the ambient seismic noise”. *Geophysical research letters* 31.7,
1062 p. L07614. DOI: [10.1029/2004GL019491](https://doi.org/10.1029/2004GL019491).
- 1063 Shapiro, N. M. and M. H. Ritzwoller (2004). “Thermodynamic constraints on seismic
1064 inversions”. *Geophysical journal international* 157.3, pp. 1175–1188. DOI: [10.1111/
1065 j.1365-246X.2004.02254.x](https://doi.org/10.1111/j.1365-246X.2004.02254.x).
- 1066 Shapiro, N. M., M. Campillo, L. Stehly, and M. H. Ritzwoller (2005). “High-resolution
1067 surface-wave tomography from ambient seismic noise”. *Science* 307.5715, pp. 1615–
1068 1618. DOI: [10.1126/science.1108339](https://doi.org/10.1126/science.1108339).
- 1069 Shen, W. and M. H. Ritzwoller (2016). “Crustal and uppermost mantle structure be-
1070 neath the United States”. *Journal of geophysical research: solid earth* 121.6, pp. 4306–
1071 4342. DOI: [10.1002/2016JB012887](https://doi.org/10.1002/2016JB012887).
- 1072 Sheng, Y., N. Nakata, and G. C. Beroza (2018). “On the nature of higher-order am-
1073 bient seismic field correlations”. *Journal of geophysical research: solid earth* 123.9,
1074 pp. 7969–7982. DOI: [10.1029/2018JB015937](https://doi.org/10.1029/2018JB015937).
- 1075 Smith, M. L. and F. A. Dahlen (1973). “The azimuthal dependence of Love and Rayleigh
1076 wave propagation in a slightly anisotropic medium”. *Journal of geophysical research*
1077 78.17, pp. 3321–3333. DOI: [10.1029/JB078i017p03321](https://doi.org/10.1029/JB078i017p03321).
- 1078 Snieder, R. (2004). “Extracting the Green’s function from the correlation of coda waves:
1079 A derivation based on stationary phase”. *Physical review e* 69.4, p. 046610. DOI:
1080 [10.1103/PhysRevE.69.046610](https://doi.org/10.1103/PhysRevE.69.046610).
- 1081 Spica, Z., M. Pertou, M. Calò, D. Legrand, F. Córdoba-Montiel, and A. Iglesias (2016).
1082 “3-D shear wave velocity model of Mexico and South US: bridging seismic networks
1083 with ambient noise cross-correlations (C^1) and correlation of coda of correlations
1084 (C^3)”. *Geophysical journal international* 206.3, pp. 1795–1813. DOI: [10.1093/gji/
1085 ggw240](https://doi.org/10.1093/gji/ggw240).

- 1086 Stehly, L., M. Campillo, B. Froment, and R. L. Weaver (2008). “Reconstructing Green’s
1087 function by correlation of the coda of the correlation (C^3) of ambient seismic noise”.
1088 *Journal of geophysical research* 113.B11, B11306. DOI: [10.1029/2008JB005693](https://doi.org/10.1029/2008JB005693).
- 1089 Tarantola, A. (2005). *Inverse problem theory and methods for model parameter esti-*
1090 *mation*. Vol. 89. Philadelphia, PA: Society for Industrial and Applied Mathematics.
1091 342 pp.
- 1092 Tian, Y. and M. H. Ritzwoller (2015). “Directionality of ambient noise on the Juan de
1093 Fuca Plate: implications for source locations of the primary and secondary micro-
- 1094 seisms”. *Geophysical journal international* 201.1, pp. 429–443. DOI: [10.1093/gji/
1095 ggv024](https://doi.org/10.1093/gji/ggv024).
- 1096 — (2017). “Improving ambient noise cross-correlations in the noisy ocean bottom en-
- 1097 vironment of the Juan de Fuca plate”. *Geophysical journal international* 210.3,
1098 pp. 1787–1805. DOI: [10.1093/gji/ggx281](https://doi.org/10.1093/gji/ggx281).
- 1099 Tian, Y., W. Shen, and M. H. Ritzwoller (2013). “Crustal and uppermost mantle shear
1100 velocity structure adjacent to the Juan de Fuca Ridge from ambient seismic noise”.
1101 *Geochemistry, geophysics, geosystems* 14.8, pp. 3221–3233. DOI: [10.1002/ggge.
1102 20206](https://doi.org/10.1002/ggge.20206).
- 1103 Toomey, D., R. Allen, A. Barclay, S. Bell, P. Bromirski, R. Carlson, X. Chen, J. Collins,
1104 R. Dziak, B. Evers, D. Forsyth, P. Gerstoft, E. Hooft, D. Livelybrooks, J. Lodewyk,
1105 D. Luther, J. McGuire, S. Schwartz, M. Tolstoy, A. Trehu, M. Weirathmueller, and
1106 W. Wilcock (2014). “The Cascadia Initiative: a sea change in seismological studies of
1107 subduction zones”. *Oceanography* 27.2, pp. 138–150. DOI: [10.5670/oceanog.2014.
1108 49](https://doi.org/10.5670/oceanog.2014.49).
- 1109 VanderBeek, B. P. and D. R. Toomey (2017). “Shallow mantle anisotropy beneath the
1110 Juan de Fuca plate”. *Geophysical research letters*. DOI: [10.1002/2017GL074769](https://doi.org/10.1002/2017GL074769).
- 1111 — (2019). “Pn tomography of the Juan de Fuca and Gorda Plates: implications for
1112 mantle deformation and hydration in the oceanic lithosphere”. *Journal of geophysical
1113 research: solid earth* 124.8, pp. 8565–8583. DOI: [10.1029/2019JB017707](https://doi.org/10.1029/2019JB017707).
- 1114 Webb, S. C. and W. C. Crawford (1999). “Long-period seafloor seismology and defor-
- 1115 mation under ocean waves”. *Bulletin of the seismological society of america* 89.6,
1116 pp. 1535–1542.
- 1117 Wilson, D. S. (1993). “Confidence intervals for motion and deformation of the Juan de
1118 Fuca Plate”. *Journal of geophysical research: solid earth* 98.B9, pp. 16053–16071.
1119 DOI: [10.1029/93JB01227](https://doi.org/10.1029/93JB01227).
- 1120 Xie, J., M. H. Ritzwoller, S. Brownlee, and B. Hacker (2015). “Inferring the oriented
1121 elastic tensor from surface wave observations: preliminary application across the
1122 western United States”. *Geophysical journal international* 201.2, pp. 996–1021. DOI:
1123 [10.1093/gji/ggv054](https://doi.org/10.1093/gji/ggv054).
- 1124 Xie, J., M. H. Ritzwoller, W. Shen, and W. Wang (2017). “Crustal anisotropy across
1125 eastern Tibet and surroundings modeled as a depth-dependent tilted hexagonally

- 1126 symmetric medium”. *Geophysical journal international* 209.1, pp. 466–491. DOI: [10.](https://doi.org/10.1093/gji/ggx004)
1127 [1093/gji/ggx004](https://doi.org/10.1093/gji/ggx004).
- 1128 Yang, Y. and M. H. Ritzwoller (2008). “Teleseismic surface wave tomography in the
1129 western U.S. using the Transportable Array component of USArray”. *Geophysical*
1130 *research letters* 35.4. DOI: [10.1029/2007GL032278](https://doi.org/10.1029/2007GL032278).
- 1131 Zhang, S., L. Feng, and M. H. Ritzwoller (2020). “Three-station interferometry and
1132 tomography: coda versus direct waves”. *Geophysical journal international* 221.1,
1133 pp. 521–541. DOI: [10.1093/gji/ggaa046](https://doi.org/10.1093/gji/ggaa046).

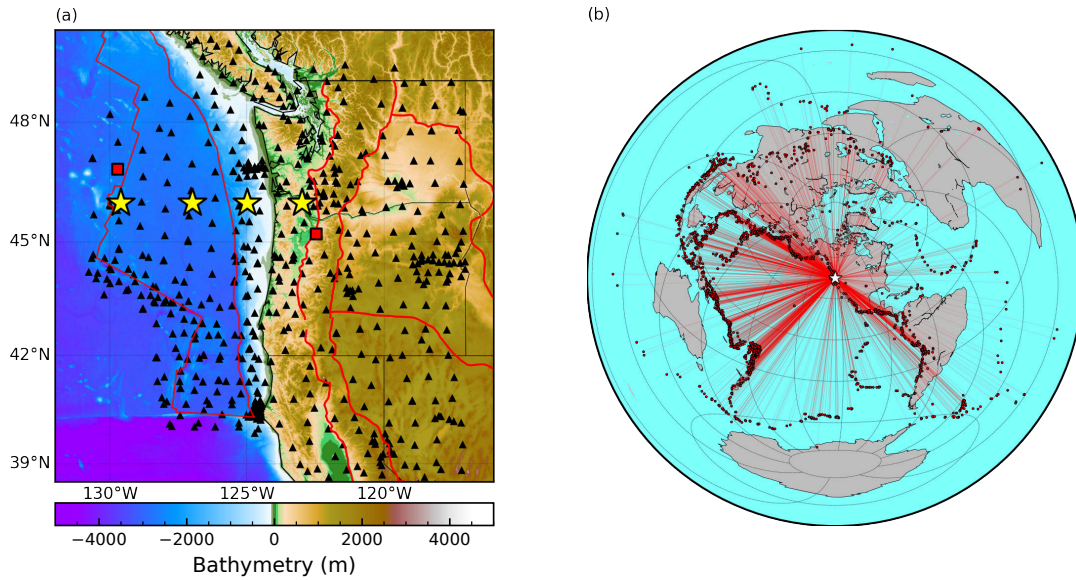


Figure 1: **Stations and earthquakes used.** (a) Region of study. Black triangles denote stations, red squares mark the pair of stations used in **Fig. 3**, and yellow stars represent example locations along 46°N referenced in **Figs 5, 16 and 15**. The background colors depict bathymetry (GEBCO Compilation Group, 2019). Red lines onshore denote physiographic provinces (Fenneman and Johnson, 1946) while red lines offshore depict plate boundaries (Bird, 2003). (b) Earthquake locations are denoted by red circles and red lines denote great circles between earthquakes and the center of the region of study (white star).

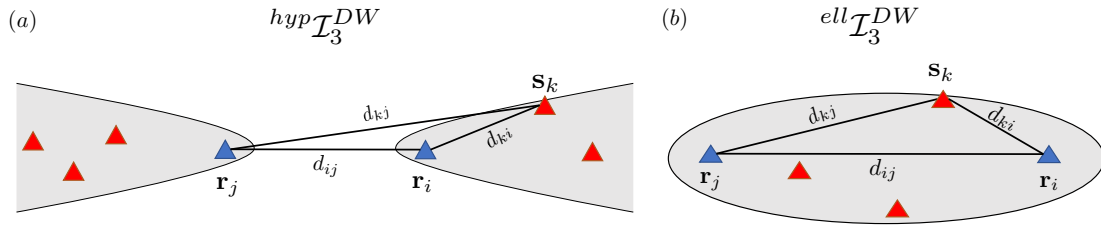


Figure 2: **Schematic representation of three-station direct-wave interferometry.** (a) For the three-station method $hyp\mathcal{I}_3^{DW}$, source-stations (s_k) are constrained to lie within a hyperbolic stationary phase zone with the receiver-stations (r_i, r_j) as foci. Two-station interferograms between s_k and r_i, r_j are correlated. Great circle distances between two stations are denoted as d with appropriate subscripts. (b) Similar to (a) but for the three-station method $ell\mathcal{I}_3^{DW}$, the source-stations are constrained to lie within an elliptical stationary phase zone, and the two-station interferograms between s_k and r_i, r_j are convolved.

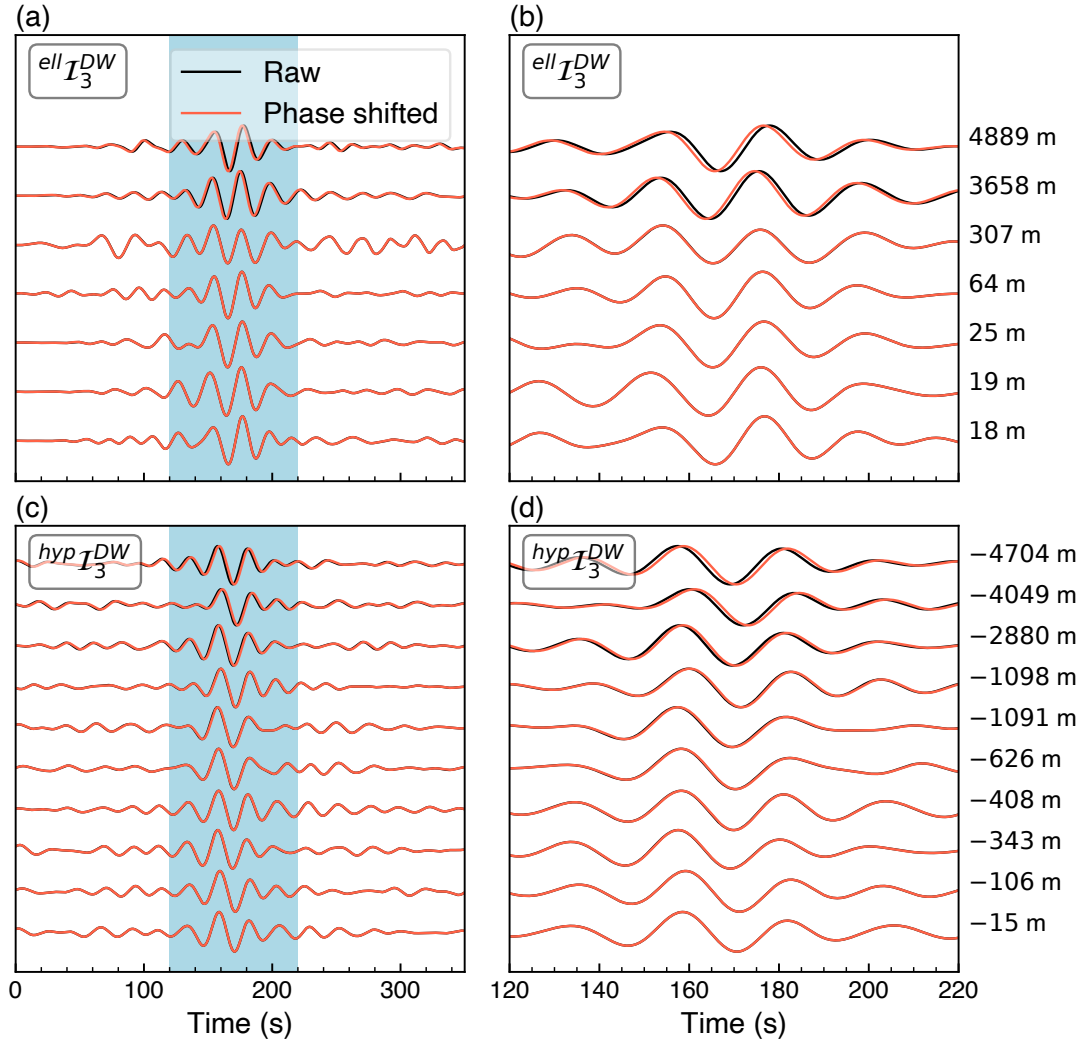


Figure 3: **De-biasing three-station direct-wave methods via phase shift.** (a) For the method $ell \mathcal{I}_3^{DW}$, to de-bias we apply a phase advance to correct for δd (eq. (4)). The source-specific interferograms are shown before (C_3 , in black) and after (\tilde{C}_3 , in red) the phase shift, respectively. The shaded areas are zoomed in (b). The traces are sorted by the values of δd which are listed to the right of each trace. (c) & (d) Similar to (a) & (b), for the method $hyp \mathcal{I}_3^{DW}$ we de-bias by applying a phase delay (eq. (3)). The receiver-stations are 7D.J47A (WHOI OBS) and UW.LCCR (Mulino, OR), and the inter-receiver distance is 589 km (Fig. 1a). All traces are low-pass filtered with a corner at 20 s period to ease visualization.

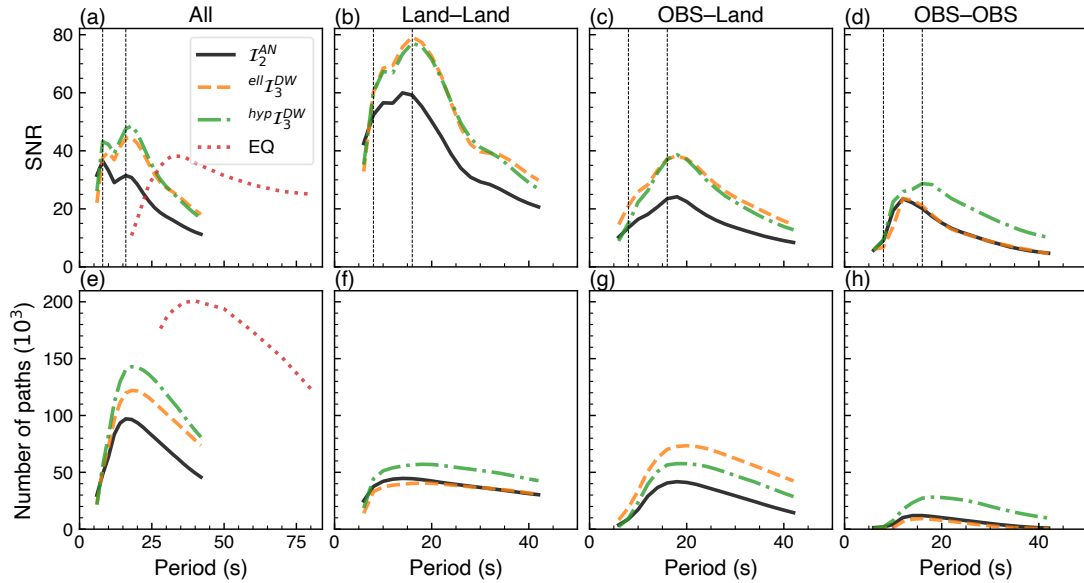


Figure 4: **Characteristics of dispersion measurements.** (a)-(d) Median of the SNR of the measurements for different methods plotted as a function of period for \mathcal{I}_2^{AN} (black), $ell\mathcal{I}_3^{DW}$ (orange), $hyp\mathcal{I}_3^{DW}$ (green), and earthquakes (red). The median values (a) are taken over all paths, (b) are for paths between a pair of land stations, (c) are between an OBS and a land station, and (d) are between a pair of OBS. Vertical lines mark the primary (~ 16 s) and secondary (~ 8 s) microseism peaks. (e)-(h) Similar to (a)-(d) but for the number of paths after quality control. The number of paths is twice that of travel time measurements for \mathcal{I}_2^{AN} , $ell\mathcal{I}_3^{DW}$ and $hyp\mathcal{I}_3^{DW}$ while the same as travel time measurements for earthquake data. Numbers presented are in thousands.

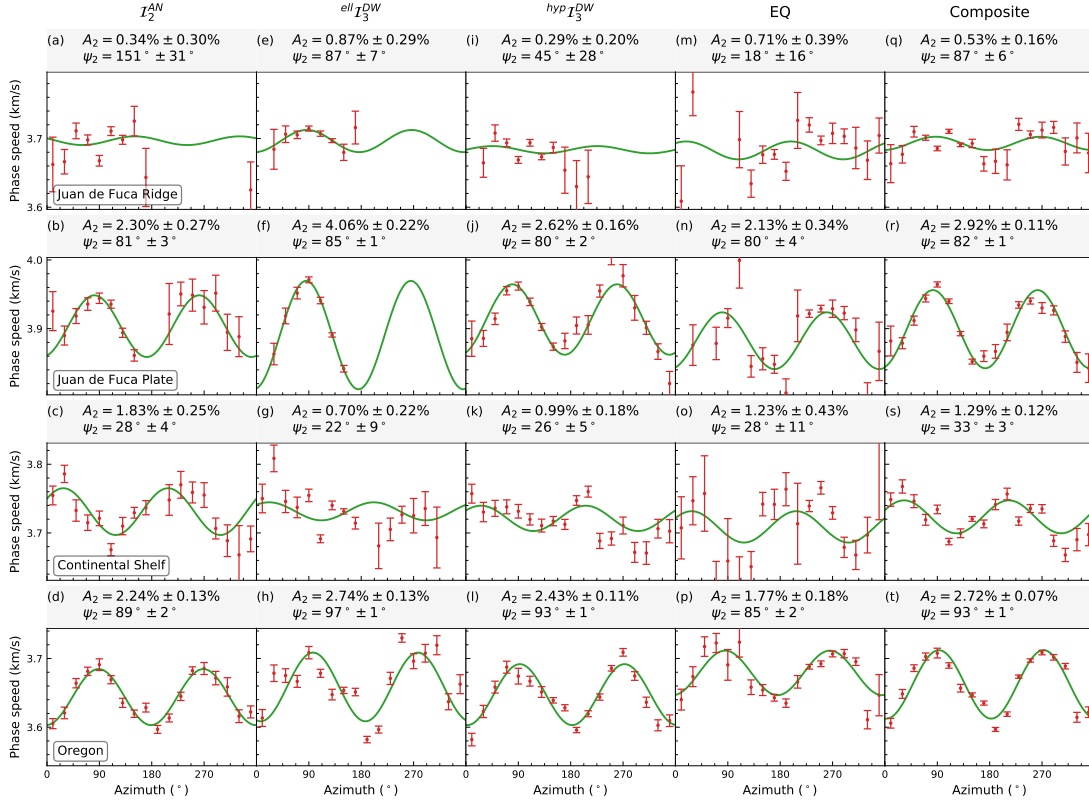


Figure 5: **Observations of azimuthal anisotropy at various locations using different methods.** Observed (red bars) and estimated (green lines) Rayleigh wave phase speed at 30 s period are plotted versus azimuth for (column 1) \mathcal{I}_2^{AN} , (column 2) $ell\mathcal{I}_3^{DW}$, (column 3) $hyp\mathcal{I}_3^{DW}$, (column 4) earthquakes, and (column 5) composite data (row 1) for a point near the Juan de Fuca Ridge, (row 2) on the Juan de Fuca Plate, (row 3) on the continental shelf east of the Juan de Fuca Plate, and (row 4) on the continent (**Fig. 1a**). Fit parameters are above each panel for 2ψ anisotropy amplitude A_2 , and 2ψ fast direction ψ_2 (eq. (12)).

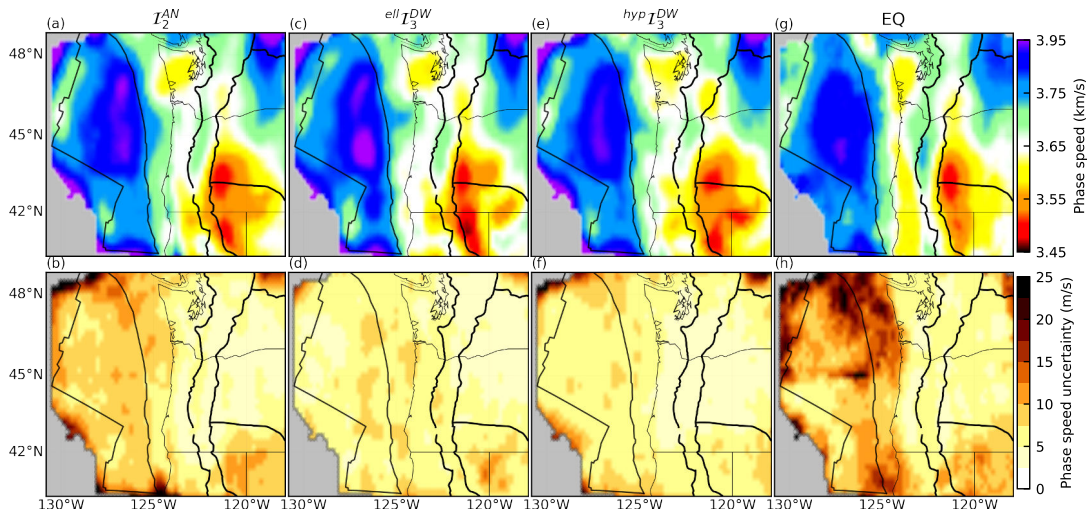


Figure 6: **Rayleigh wave isotropic phase speed maps at 30 s period from different methods.** (a) Phase speed map \bar{c} using \mathcal{I}_2^{AN} and (b) associated uncertainties $\sigma_{\bar{c}}$. (c)-(h) Similar to (a) & (b) except based on (c) & (d) $ell\mathcal{I}_3^{DW}$, (e) & (f) $hyp\mathcal{I}_3^{DW}$, and (g) & (h) earthquakes (EQ).

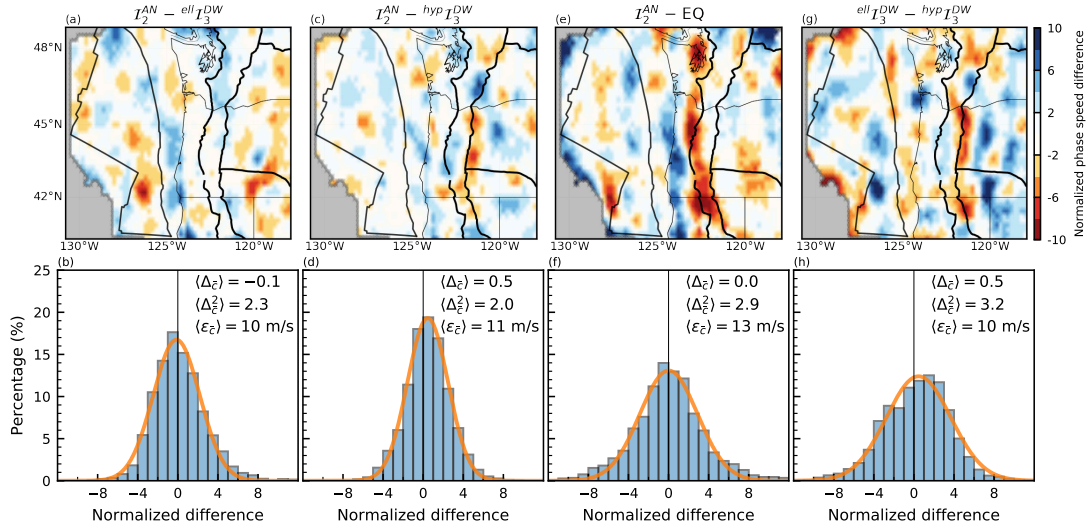


Figure 7: **Normalized differences between 30 s Rayleigh wave isotropic phase speed maps (Fig. 6) from different methods.** (a) Normalized difference $\Delta_{\bar{c}}$ (eq. 14) between results from \mathcal{I}_2^{AN} and $ell \mathcal{I}_3^{DW}$. (b) Histogram taken over the spatial nodes of (a). The orange line denotes a Gaussian fit to the histogram. The spatial mean $\langle \Delta_{\bar{c}} \rangle$ and standard deviation $\langle \Delta_{\bar{c}}^2 \rangle$ of $\Delta_{\bar{c}}$, and the spatial mean of the combined uncertainties $\langle \epsilon_{\bar{c}} \rangle$ (eq. 13) are listed on the upper right corner. (c)-(h) Similar to (a) & (b) except the comparison in (c) & (d) is based on $hyp \mathcal{I}_3^{DW}$ and \mathcal{I}_2^{AN} , in (e) & (f) it is based on earthquake data (EQ) and \mathcal{I}_2^{AN} , and in (g) & (h) it is based on $ell \mathcal{I}_3^{DW}$ and $hyp \mathcal{I}_3^{DW}$.

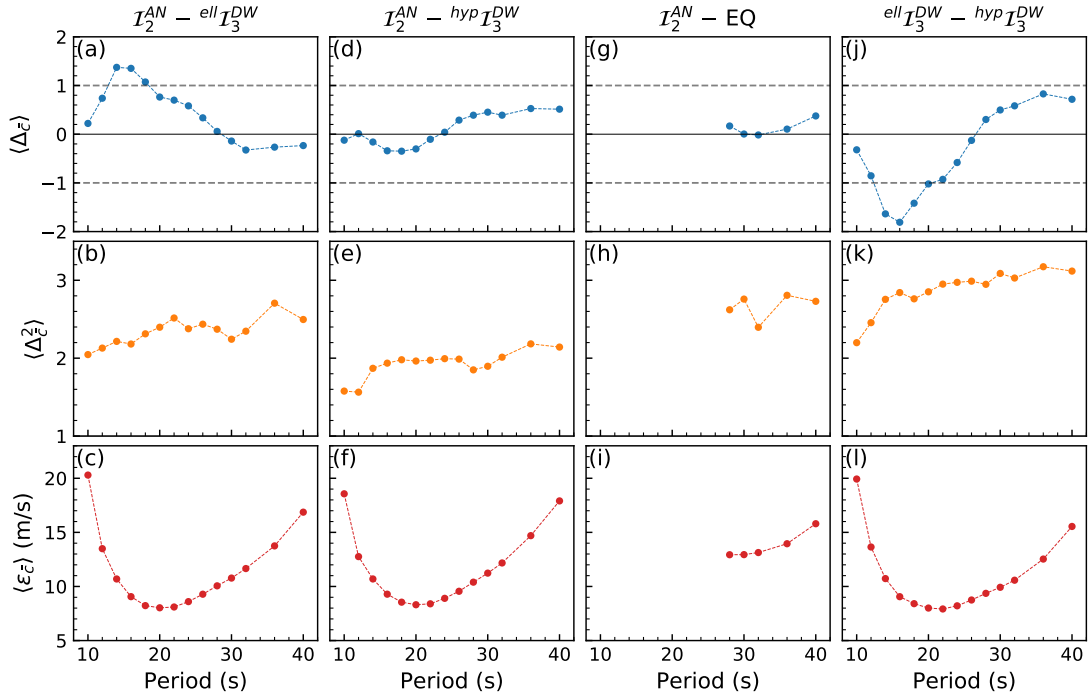


Figure 8: **Statistics of period-dependent differences between the isotropic phase speed maps from different methods.** (a) & (b) The differences are spatial means $\langle \Delta_{\bar{\epsilon}} \rangle$ and standard deviations $\langle \Delta_{\bar{\epsilon}}^2 \rangle$ of the normalized difference $\Delta_{\bar{\epsilon}}$ (eq. 14) between \mathcal{I}_2^{AN} and $ell\mathcal{I}_3^{DW}$, with (c) associated spatial mean of combined uncertainties $\langle \epsilon_{\bar{\epsilon}} \rangle$ (eqs. (14)–(16)). (d)–(l) Similar to (a) – (c) except the comparison in (d) – (f) is based on $hyp\mathcal{I}_3^{DW}$ and \mathcal{I}_2^{AN} , in (g) – (i) it is based on earthquake data (EQ) and \mathcal{I}_2^{AN} , and in (j) & (l) it is based on $ell\mathcal{I}_3^{DW}$ and $hyp\mathcal{I}_3^{DW}$.

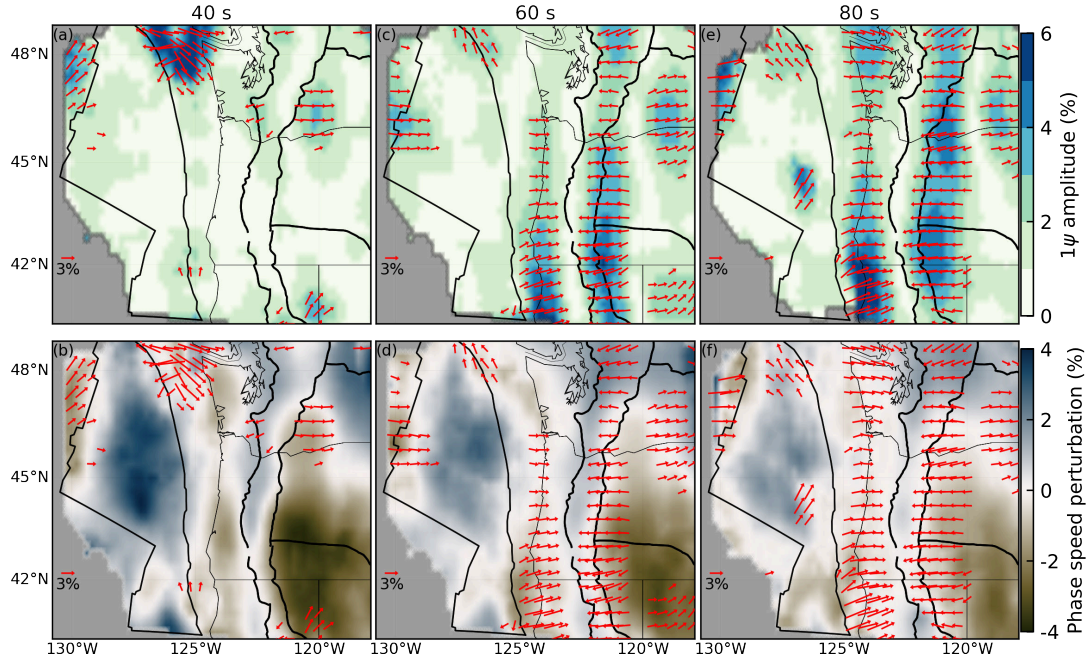


Figure 9: **Observation of apparent 1ψ azimuthal anisotropy.** (a) & (b) At 40 s period, (a) the red arrows point in the fast direction of 1ψ anisotropy, ψ_1 , with lengths proportional to the peak-to-peak 1ψ amplitudes, A_1 (eq. (12)). The arrows are drawn only where $A_1 > 2\%$. The background map depicts A_1 . (b) The arrows are the same as in (a) but the background map depicts the perturbation of isotropic phase speed A_0 from the mean. (c)-(f) Similar to (a) & (b) but at (c) & (d) 60 s period and (e) & (f) 80 s period.

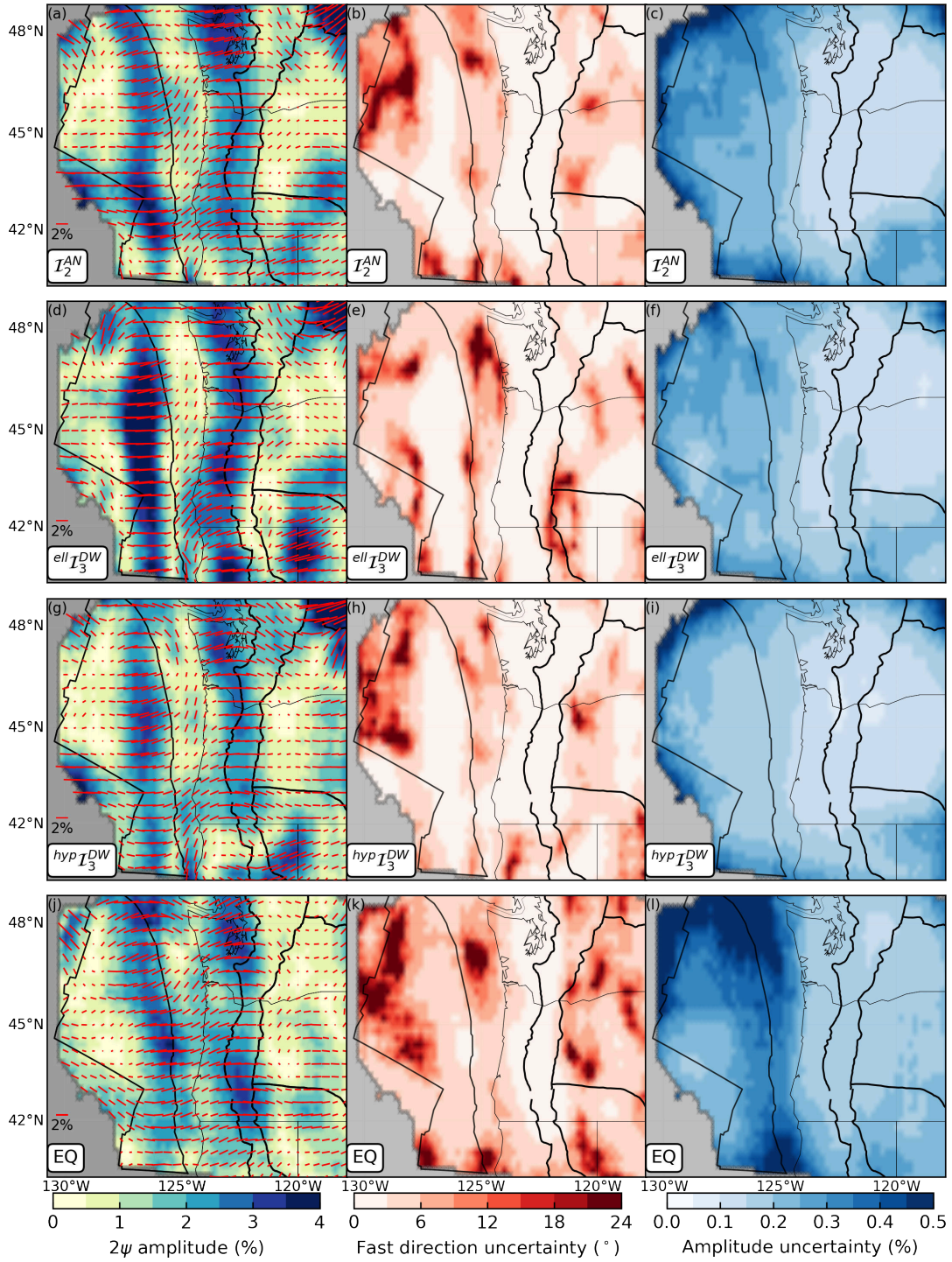


Figure 10: **Rayleigh wave 2ψ azimuthal anisotropy maps at 30 s period from different methods.** (a)-(c) Based on \mathcal{I}_{242}^{AN} , (a) 2ψ peak-to-peak amplitudes A_2 (eq. (12)) and fast directions ψ_2 are represented by the lengths and directions of red bars, respectively. The background map depicts A_2 . The associated uncertainties are shown for (b) ψ_2 and (c) A_2 . (d)-(l) Similar to (a)-(c) except based on (d)-(f) $ell \mathcal{I}_3^{DW}$, (g)-(i) $hyp \mathcal{I}_3^{DW}$, and (j)-(l) earthquake data.

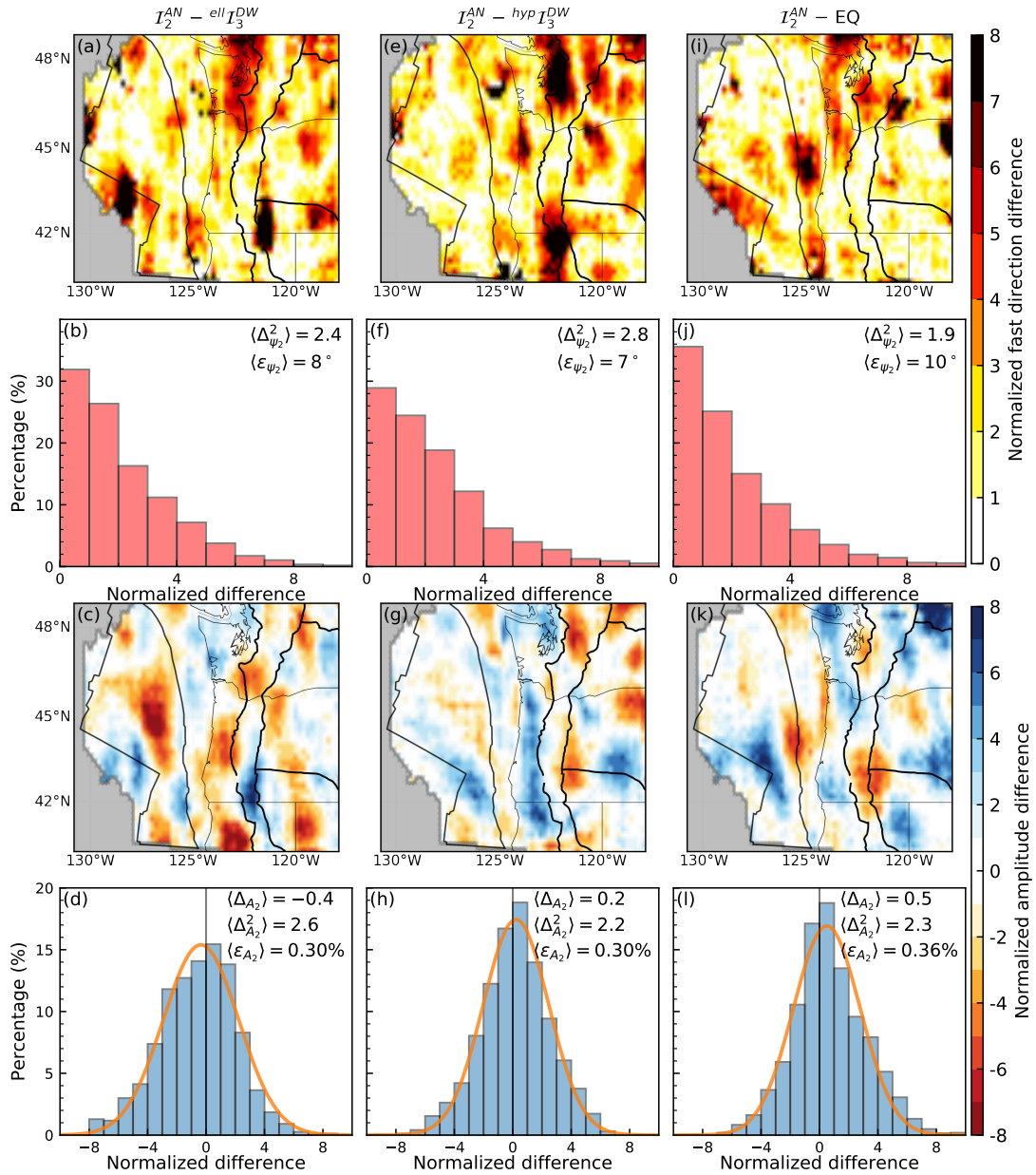


Figure 11: Comparison of the 30 s period Rayleigh wave 2ψ azimuthal anisotropy maps (Fig. 10) based on different methods. (a) Normalized absolute difference of 2ψ fast directions (Δ_{ψ_2}) between \mathcal{I}_2^{AN} and $ell \mathcal{I}_3^{DW}$. (b) Histogram of (a). The spatial standard deviation of the normalized difference $\langle \Delta_{\psi_2}^2 \rangle$ and the spatial mean of the combined uncertainties $\langle \epsilon_{\psi_2} \rangle$ are listed in the upper right corner. (c) & (d) Similar to (a) & (b) except the difference is for 2ψ amplitudes, A_2 . The orange line in (d) is the Gaussian fit to the histogram and the spatial mean of the normalized difference $\langle \Delta_{A_2} \rangle$ is also listed. (e)-(l) Similar to (a)-(d), except the difference is (e)-(h) between \mathcal{I}_2^{AN} and $hyp \mathcal{I}_3^{DW}$, and (i)-(l) between \mathcal{I}_2^{AN} and earthquake data (EQ).

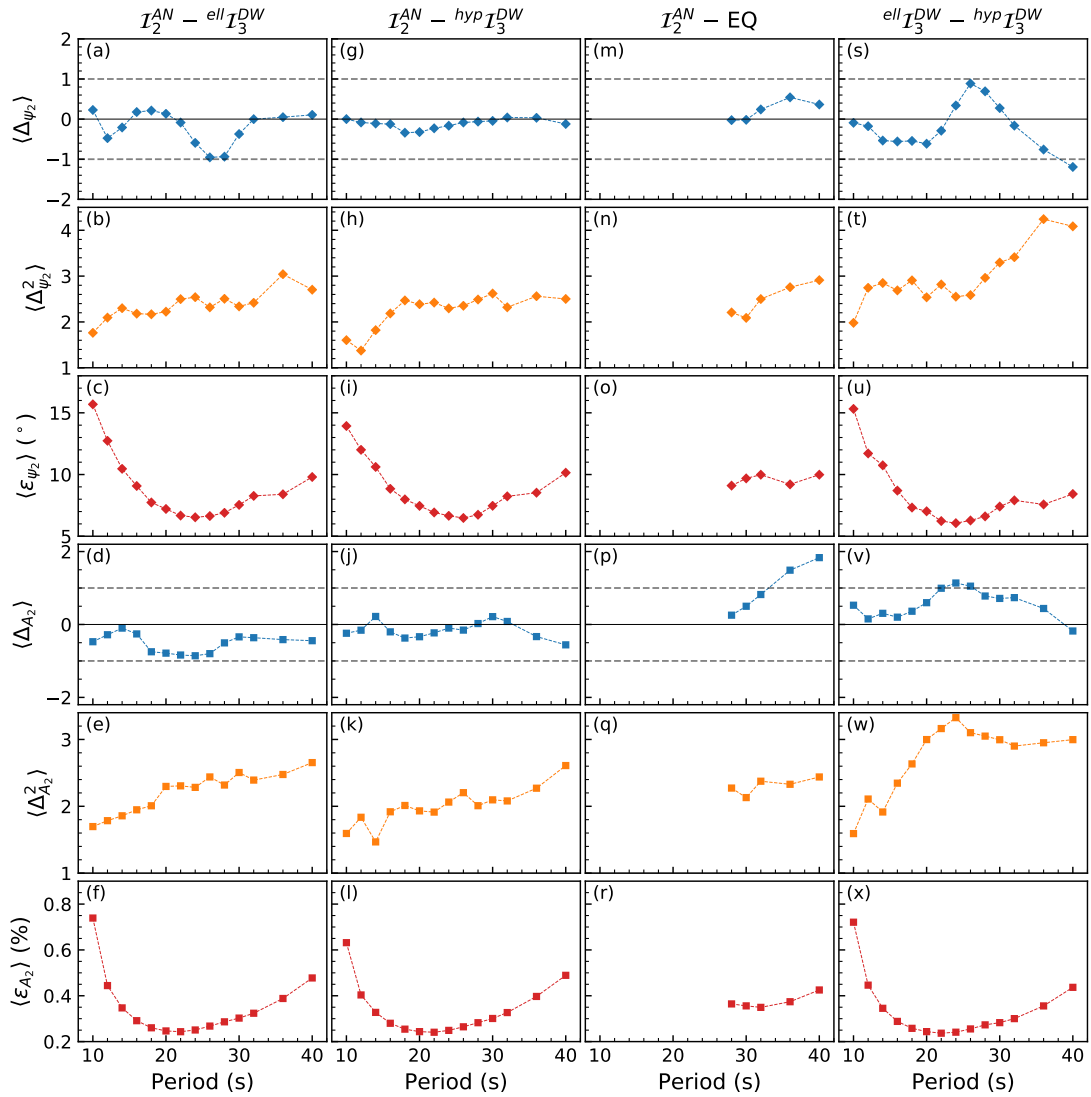


Figure 12: **Statistics of period-dependent differences between the anisotropic maps from different methods.** (a)-(c) The statistics are spatial (a) means $\langle \Delta_{\psi_2} \rangle$ and (b) standard deviations $\langle \Delta_{\psi_2}^2 \rangle$ of the normalized difference in fast directions Δ_{ψ_2} (eq. (14)) between \mathcal{I}_2^{AN} and $ell\mathcal{I}_3^{DW}$, and (c) is the associated spatial mean of combined uncertainties $\langle \epsilon_{\psi_2} \rangle$. (d)-(f) Similar to (a)-(c) except the statistics are for amplitudes A_2 . (g)-(x) Similar to (a)-(f) except in (g)-(l) the comparison is based on $hyp\mathcal{I}_3^{DW}$ and \mathcal{I}_2^{AN} , in (m)-(r) it is based on earthquake data (EQ) and \mathcal{I}_2^{AN} , and in (s)-(x) it is based on $ell\mathcal{I}_3^{DW}$ and $hyp\mathcal{I}_3^{DW}$.

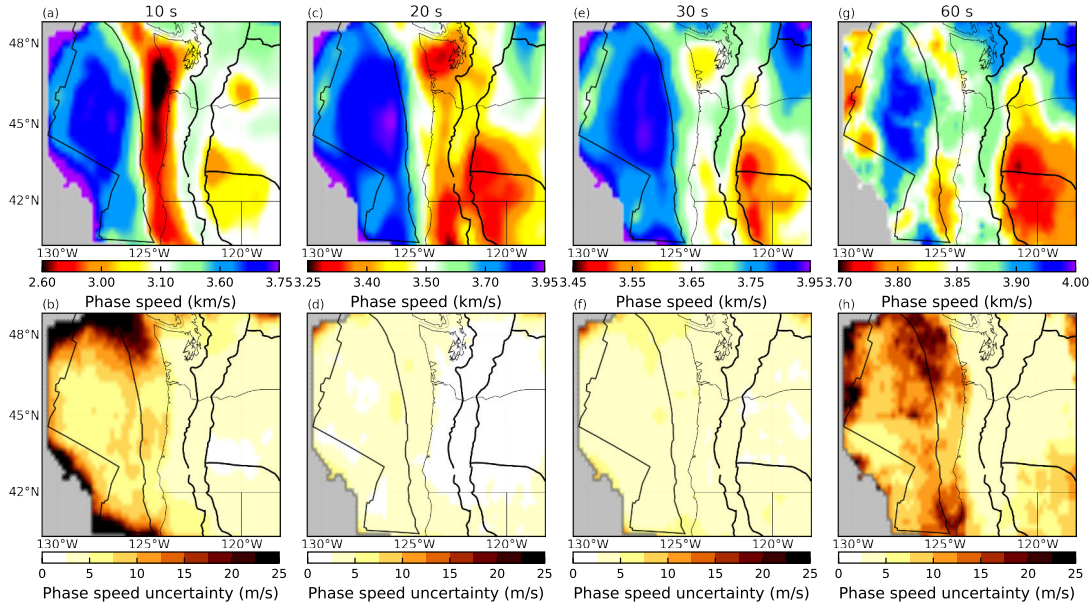


Figure 13: **Composite Rayleigh wave isotropic phase speed maps at several periods.** (a) Phase speed map \bar{c} at 10 s period combining data from \mathcal{I}_2^{AN} , $ell\mathcal{I}_3^{DW}$ and $hyp\mathcal{I}_3^{DW}$ with (b) associated uncertainties $\sigma_{\bar{c}}$. (c) & (d) Similar to (a) & (b) except at 20 s period. (e) & (f) Similar to (a) & (b) except at 30 s period. At this period, earthquake data also contribute. (g) & (h) Similar to (a) & (b) except at 60 s period where only earthquake data are available.

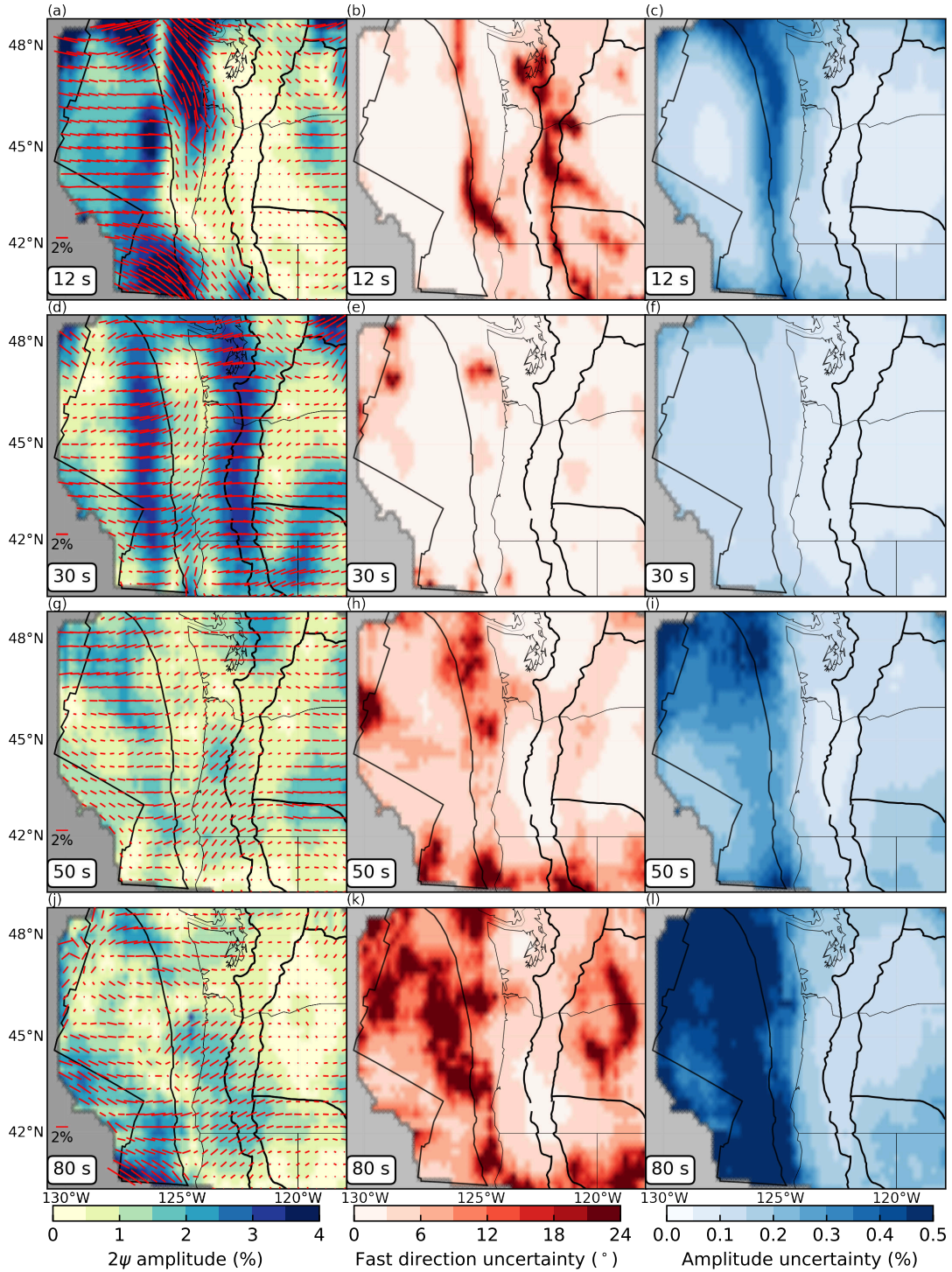


Figure 14: **Composite 2ψ azimuthal anisotropy maps at several periods.** (a)-(c) Similar to **Figs 10a-c** but based on combined data from \mathcal{I}_2^{AN} , $ell\mathcal{I}_3^{DW}$ and $hyp\mathcal{I}_3^{DW}$ at 12 s period. (d)-(f) Similar to (a)-(c) except at 30 s period earthquake data are also available. (g)-(i) Similar to (a)-(c) except (g)-(i) at 50 s period and (j)-(l) at 80 s period, only earthquake data are available.

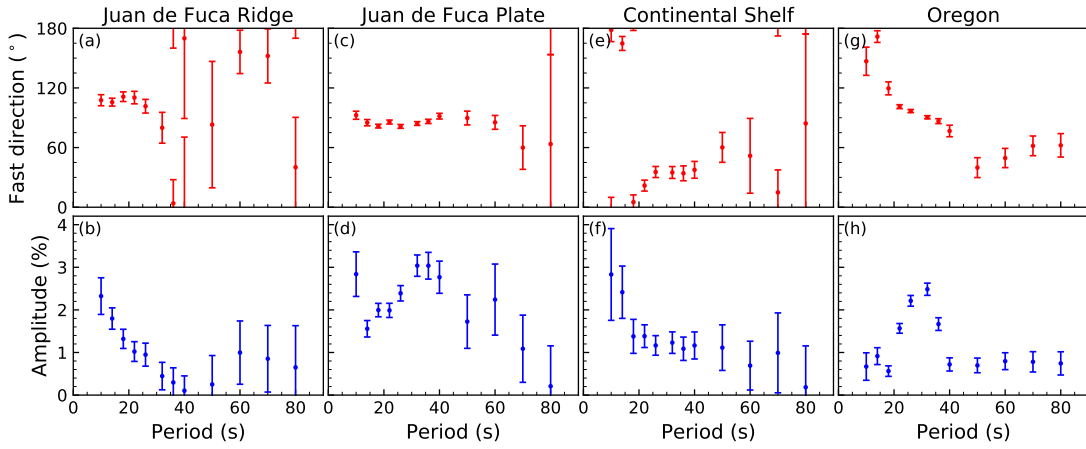


Figure 15: **Local period-dependent Rayleigh wave azimuthally anisotropic dispersion curves.** (a) Fast directions and (b) peak-to-peak amplitudes for 2ψ anisotropy versus period for a point near the Juan de Fuca Ridge. Error bars are the mean \pm twice the uncertainties: $\psi_2 \pm 2\sigma_{\psi_2}$ and $A_2 \pm 2\sigma_{A_2}$. Only earthquake data are available at periods > 40 s. (c)-(h) Similar to (a) & (b) except (c) & (d) on the Juan de Fuca Plate, (e) & (f) on the continental shelf east of the Juan de Fuca Plate, and (g) & (h) on the continent (**Fig. 1a**).

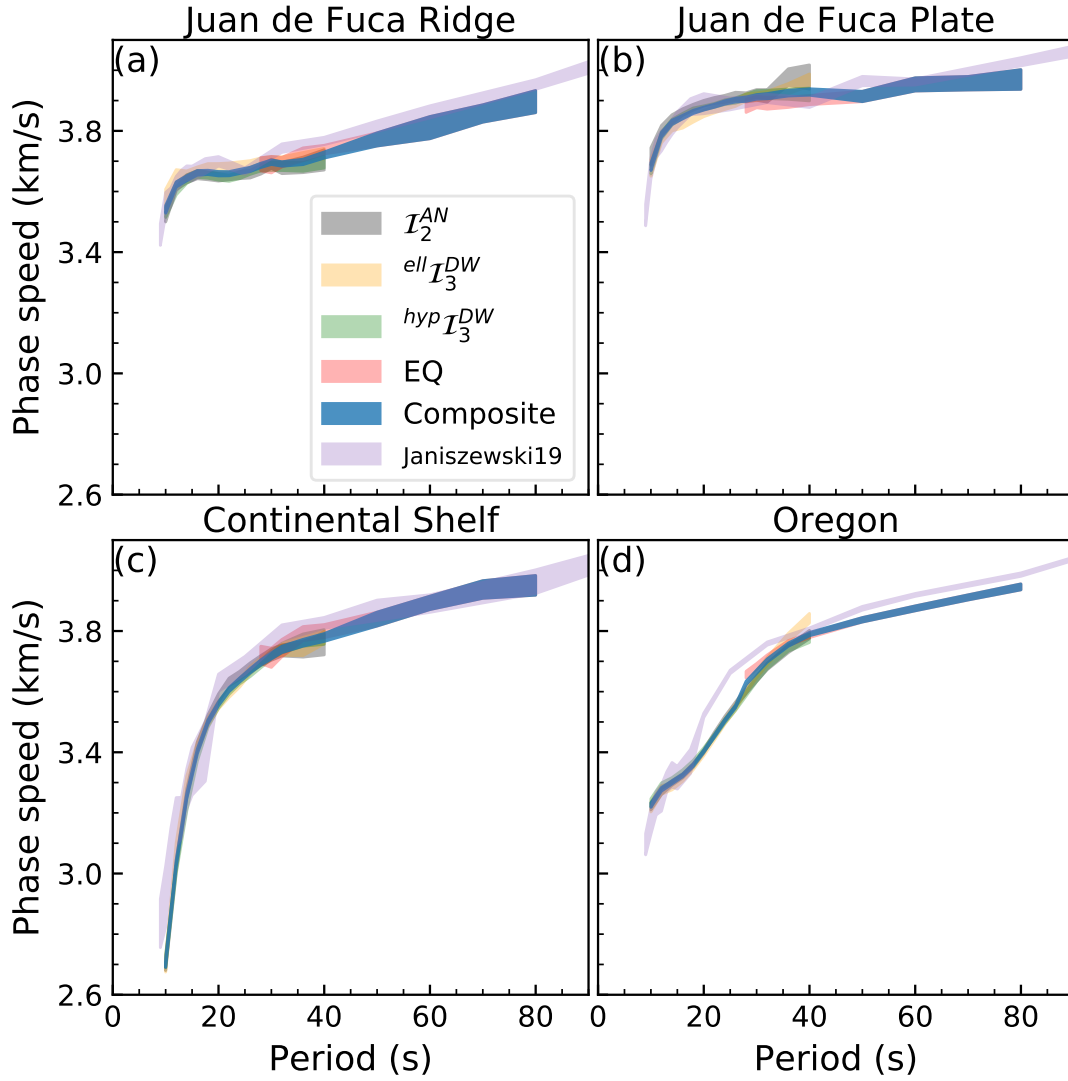


Figure 16: **Local Rayleigh wave isotropic dispersion curves.** Local dispersion curves are plotted for a point (a) near the Juan de Fuca Ridge, (b) on the Juan de Fuca Plate, (c) on the continental shelf, and (d) on the continent (**Fig. 1a**) from \mathcal{I}_2^{AN} (gray), $ell \mathcal{I}_3^{DW}$ (red), $hyp \mathcal{I}_3^{DW}$ (green), earthquake data (orange), composite data (blue), and Janiszewski et al. (2019) (light purple). The shadings represent $\bar{c} \pm 2\sigma_{\bar{c}}$.

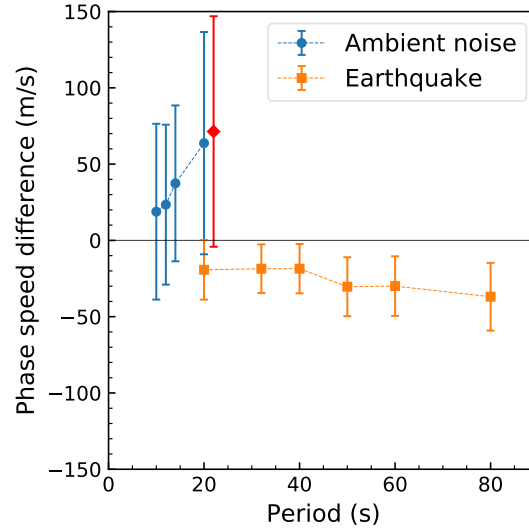


Figure 17: **Comparison of isotropic phase speed maps with those from Janiszewski et al. (2019).** Error bars denote the spatial mean of the raw difference \pm combined uncertainties $\langle \epsilon_{\bar{c}} \rangle$. Maps of Janiszewski et al. (2019) are from ambient noise at periods ≤ 20 s (blue circles) and from earthquake data at periods ≥ 20 s (orange squares). The red error bar is the difference between their ambient noise and earthquake results at 20 s (slightly shifted from 20 s for visualization). These results can be compared approximately to differences in the maps produced by our methods by multiplying $\langle \Delta_{\bar{c}} \rangle$ and $\langle \epsilon_{\bar{c}} \rangle$ from **Fig. 8**.

1 **Supporting Information for**
2 Isotropic and Azimuthally Anisotropic Rayleigh Wave
3 Dispersion Across the Juan de Fuca and Gorda Plates and U.S.
4 Cascadia from Earthquake Data and Ambient Noise Two- and
5 Three-Station Interferometry

6 Shane Zhang^{*1}, Hongda Wang¹, Mengyu Wu¹, and Michael H. Ritzwoller¹

7 ¹ Department of Physics, University of Colorado Boulder, Boulder, CO 80309, USA.

8 **Contents of this file**

9 Table [S1](#)

10 Figures [S1](#) to [S10](#)

11 **Introduction**

12 **Table S1** summarizes problematic stations identified. Using ambient noise travel time
13 residuals between a priori phase speed maps (e.g. **Fig. 13** of the main paper) and measure-
14 ments, instruments with π phase shift, mislocation, or unknown errors are identified (**Fig.**
15 **S1**). By comparing amplitudes from the same earthquake at nearby stations ($< \sim 100$ km),
16 instrument gain problems are detected (**Fig. S2**). Because nearby stations are not always
17 available, our detection of gain problems is probably incomplete. A more comprehensive ap-
18 proach may be to compare amplitudes between synthetics and measurements (e.g. Ekström
19 and Nettles, 2018).

20 **Figs S3–S10** present detailed comparisons between our Rayleigh wave isotropic phase
21 speed maps and Janiszewski et al. (2019). The statistics of the differences are summarized in
22 **Fig. 12** of the main paper.

*shzh3924@colorado.edu

23 **Table S1**

Table S1: Problematic Stations

Problem	Instrument type	Identified before? ⁱ	Station
π shift ^a	land	–	CN.HOPB
	LDEO	Y	7D.G02D
		N	Z5.* ^e
Mislocation ^a	land	–	NV.NCBC
	LDEO	N	7D.FN08C, 7D.FN11C
		SIO	N
Unknown ^a	LDEO	N	7D.M10B, 7D.M18B
		SIO	7D.M04C
Gain ^b	LDEO ^c	Y	CI yrs 1–3 ^f
		N	7D.FC03D, 7D.FS45D, 7D.G18D, 7D.G34D, 7D.J09D, 7D.J10D, 7D.J17D, 7D.J18D, 7D.M15D, 7D.M17D,
			Z5.GB100
	SIO ^d	N	7D.J23D, Z5.BB830, Z5.GB111, Z5.GB171
			7D.J68A ^g
			X9.BB320 ^h
WHOI	N		

^a Identified from ambient noise station travel time residuals and are not corrected.

^b Identified by comparing earthquake amplitudes at nearby stations ($< \sim 100$ km).

^c A correction factor of 2.37 is applied (Janiszewski et al., 2019).

^d A correction factor of 0.2 is applied.

^e All stations in the Z5 network.

^f Cascadia Initiative deployment years 1–3.

^g Uncorrected due to unknown factor.

^h Uncorrected due to temporal variability.

ⁱ Janiszewski et al. (2019).

24 **Figures S1 to S10**

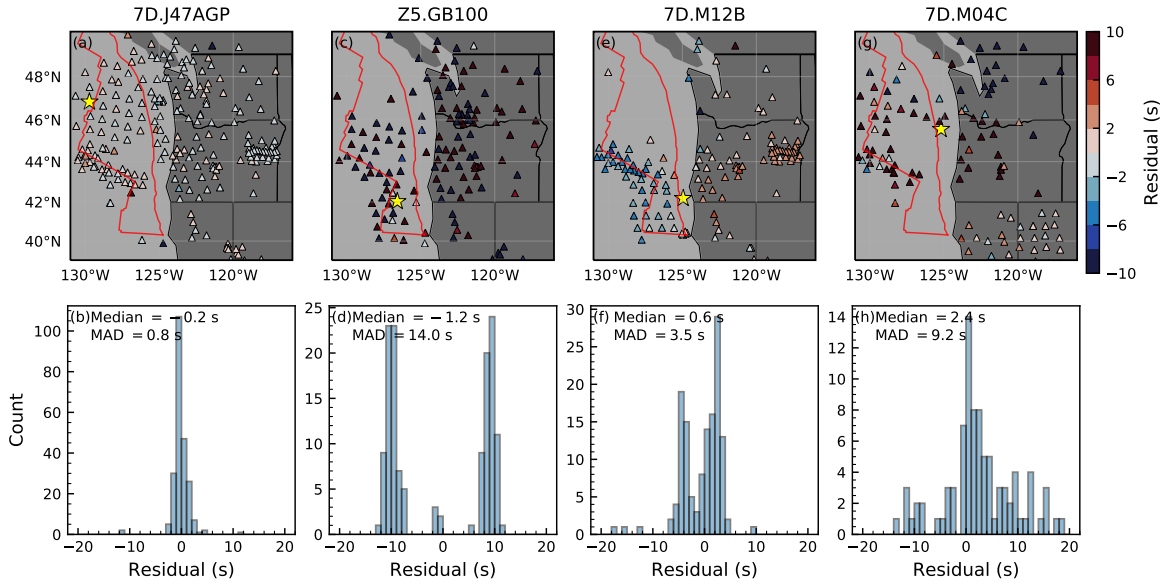


Figure S1: **Examples of travel time residuals for identification of problematic stations.** (a) For a normal station 7D.J47AGP (7D.J47A & 7D.J47C, yellow star), travel time residuals at 20 s period with other stations (triangles) are shown. (b) Histogram of residuals in (a) whose median and MAD are labeled in the upper left. (c) & (d) Similar to (a) & (b) except for a station with π phase shift. (e) & (f) Similar to (a) & (b) except for a station probably mislocated. (g) & (h) Similar to (a) & (b) except for a station with unknown problems.

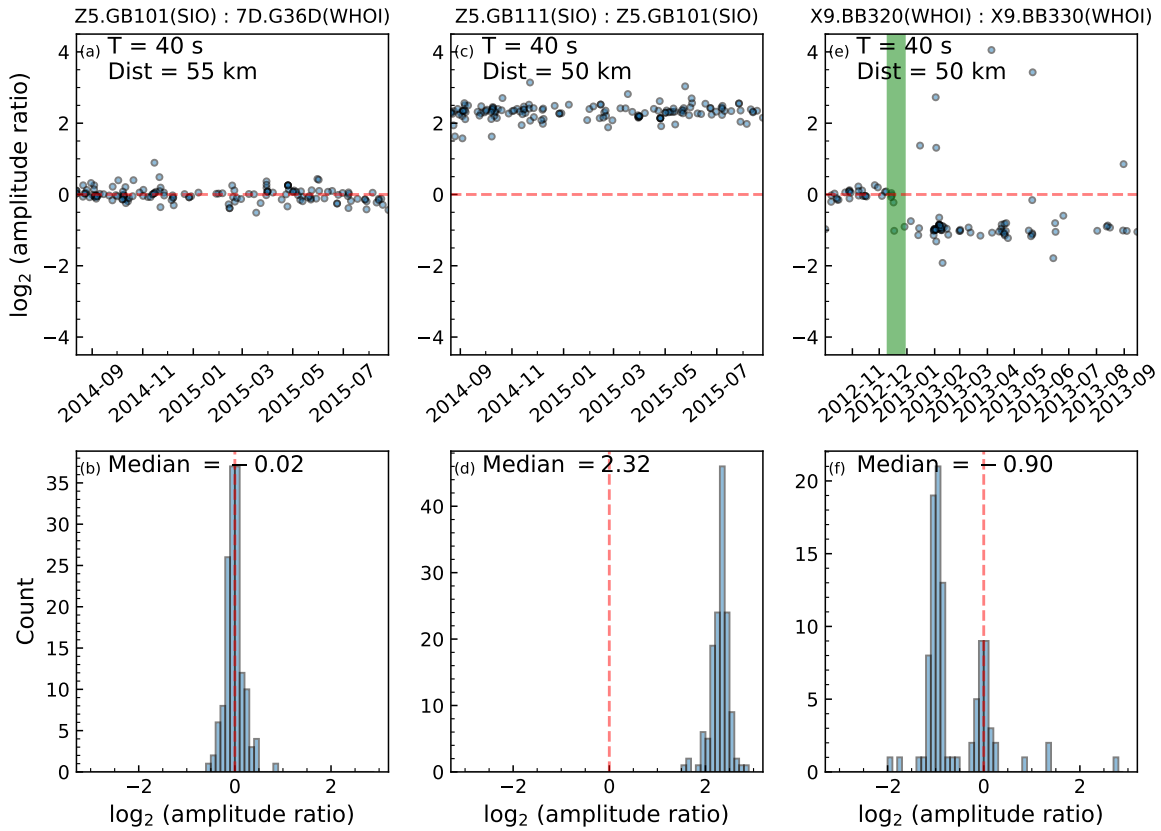


Figure S2: **Examples of amplitude ratios for identification of instrument gain problems.** (a) For a normal station Z5.GB101, the amplitude ratios at 40 s period from the same earthquakes with another normal station (7D.G36D) which is 55 km apart are plotted against the dates of the earthquakes. (b) Histogram of ratios in (a) whose median is -0.02 . (c) & (d) Similar to (a) & (b) except for a station with (time-independent) overestimation of amplitudes. (e) & (f) Similar to (a) & (b) except for a station with time-variable gain, where the discontinuity around Dec 2012 is highlighted in green.

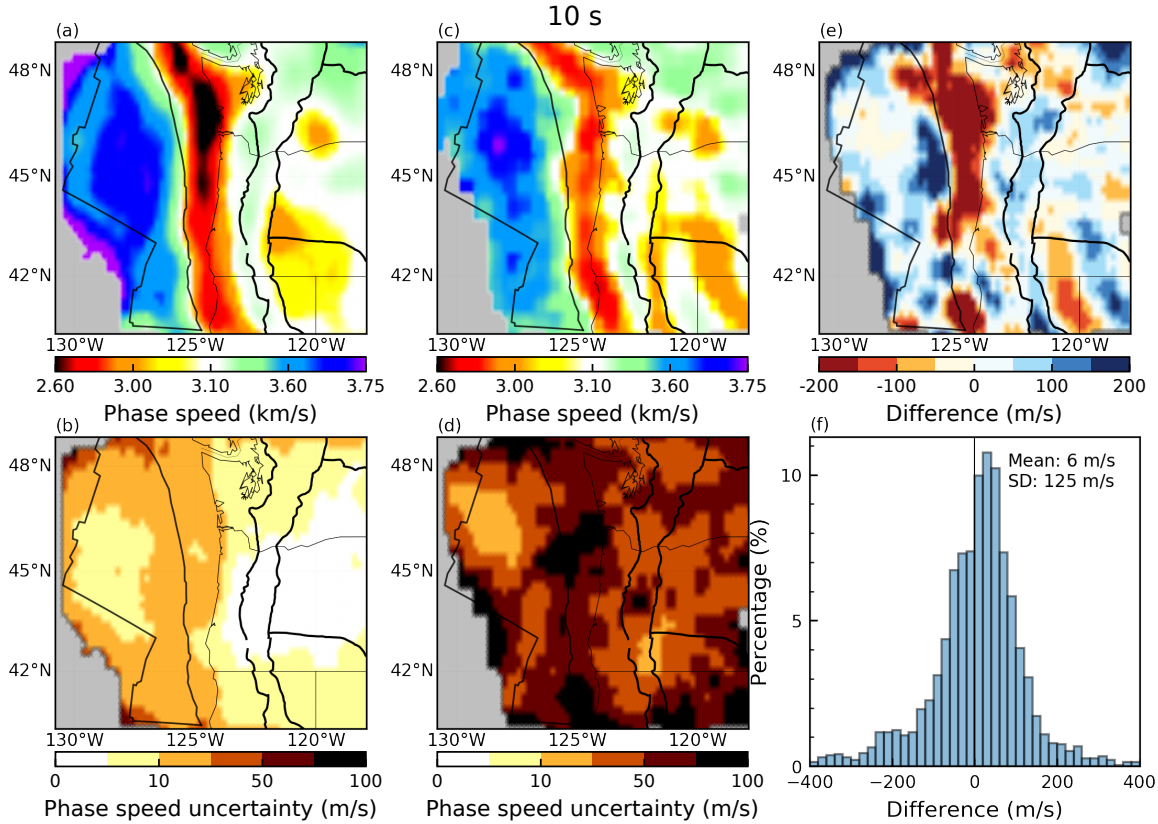


Figure S3: **Comparison of Rayleigh wave isotropic phase speed map at 10 s period with Janiszewski et al. (2019).** (a) & (b) Our phase speed map and associated errors combining two- and three-station interferometry. (c) & (d) Similar to (a) & (b) except from Janiszewski et al. (2019) using two-station interferometry. (e) Normalized difference between (a) and (c) where a positive number means our map is faster. (f) Histogram of (e). The mean and the standard deviation are labeled in the upper right.

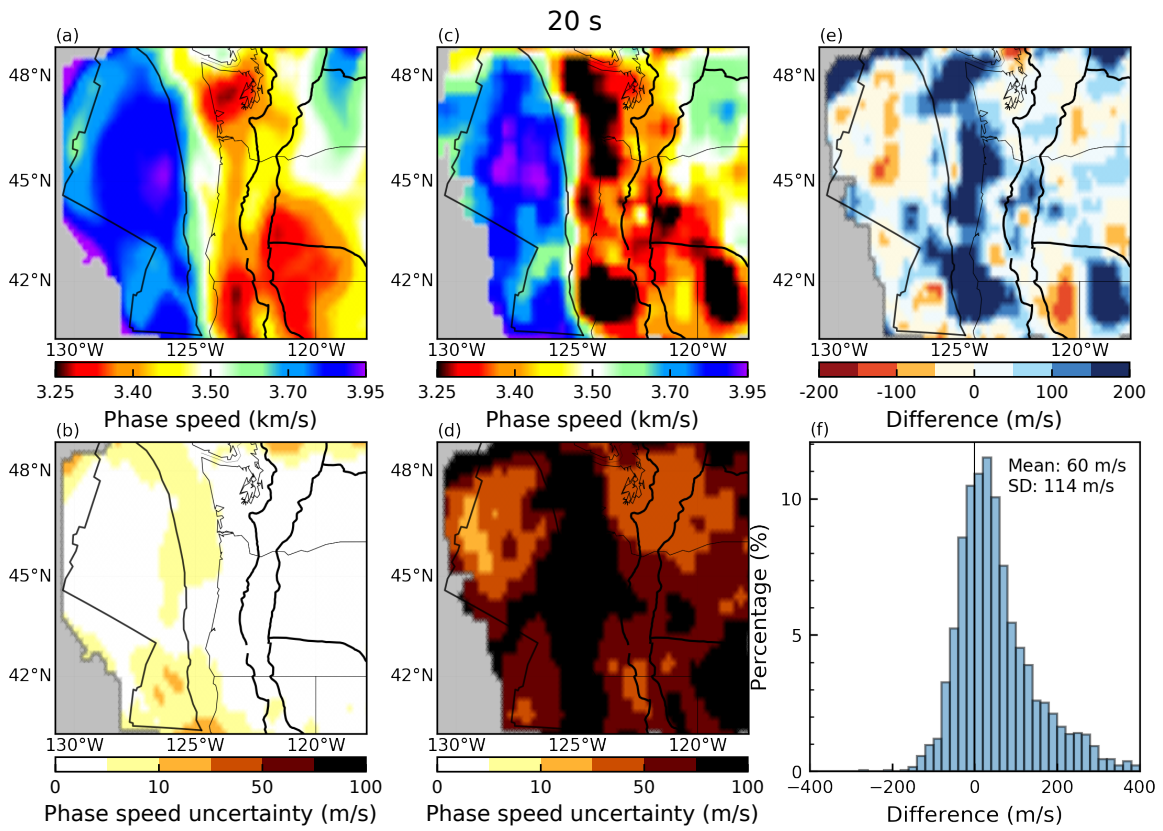


Figure S4: Same as Fig. S3 except at 20 s period. (c) (d) Maps of Janiszewski et al. (2019) are from ambient noise two-station interferometry.

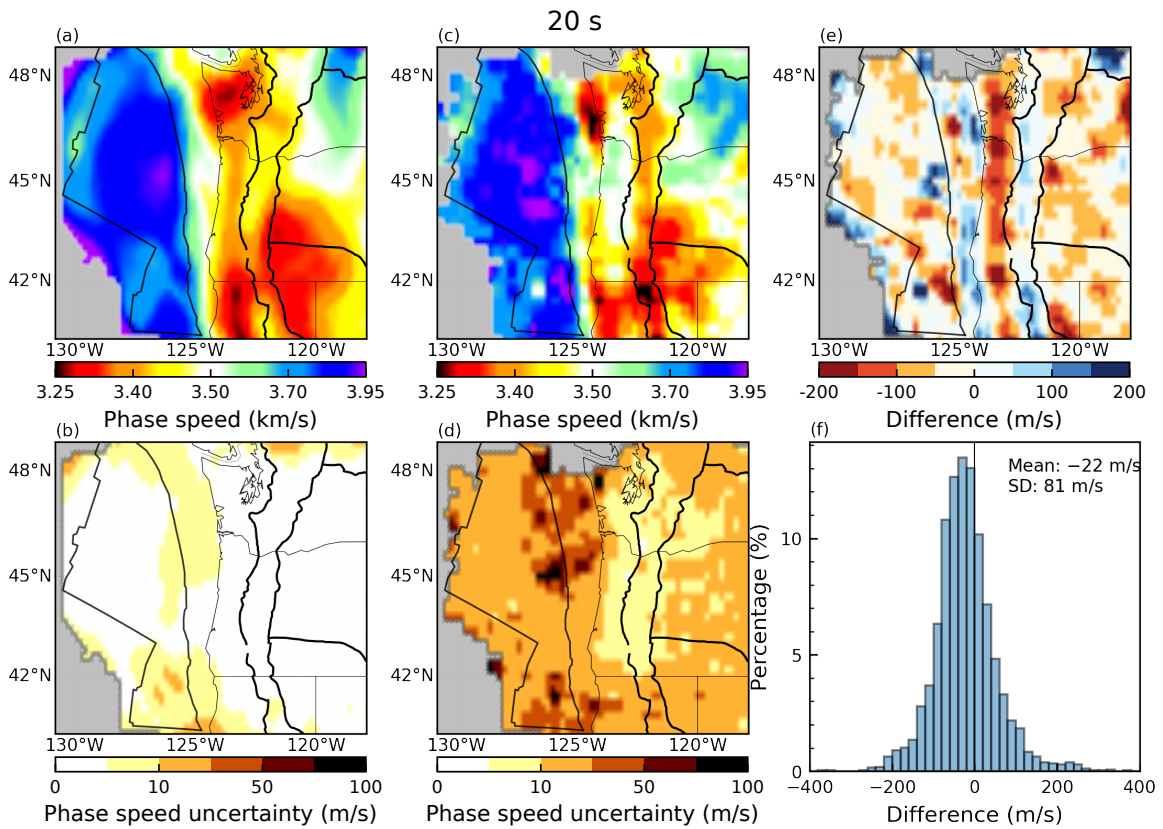


Figure S5: Same as Fig. S4 except (c) & (d) maps of Janiszewski et al. (2019) are from earthquakes.

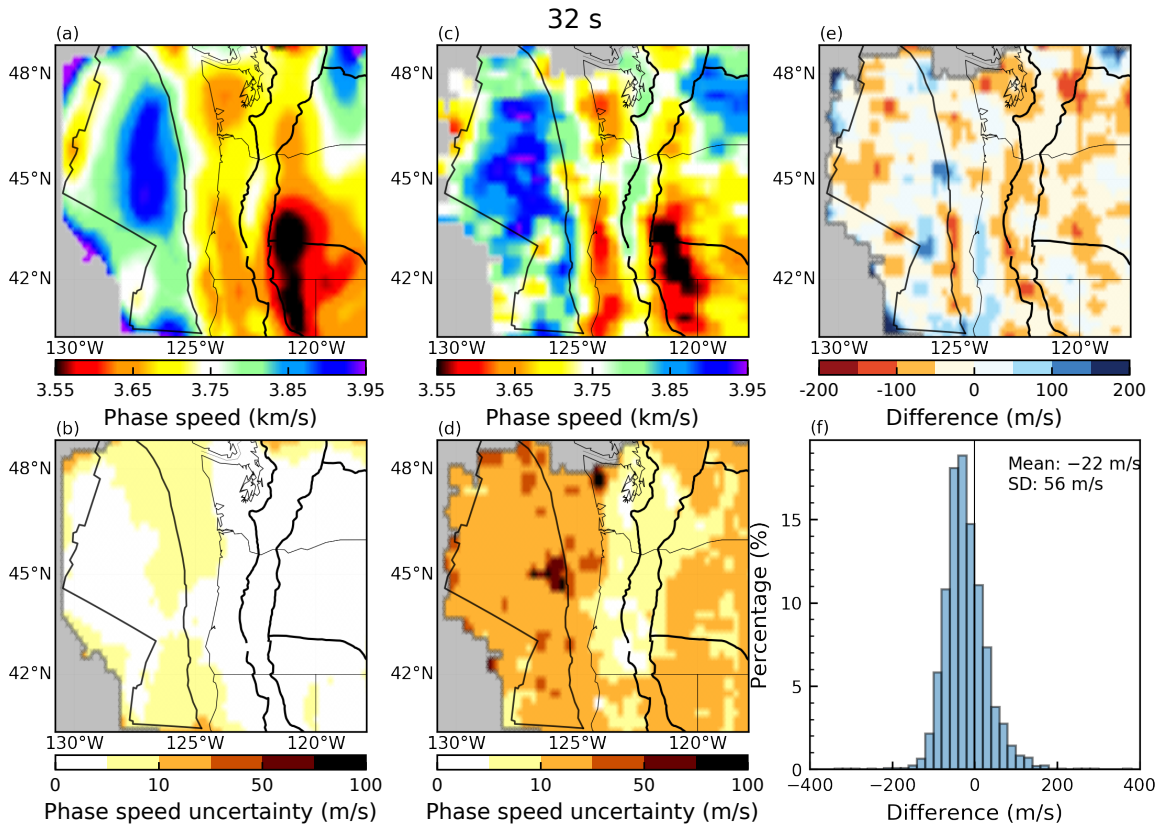


Figure S6: **Similar to Fig. S5 except at 32 s period.** (a) & (b) Our maps combine two-station interferometry, three-station interferometry, and earthquake data.

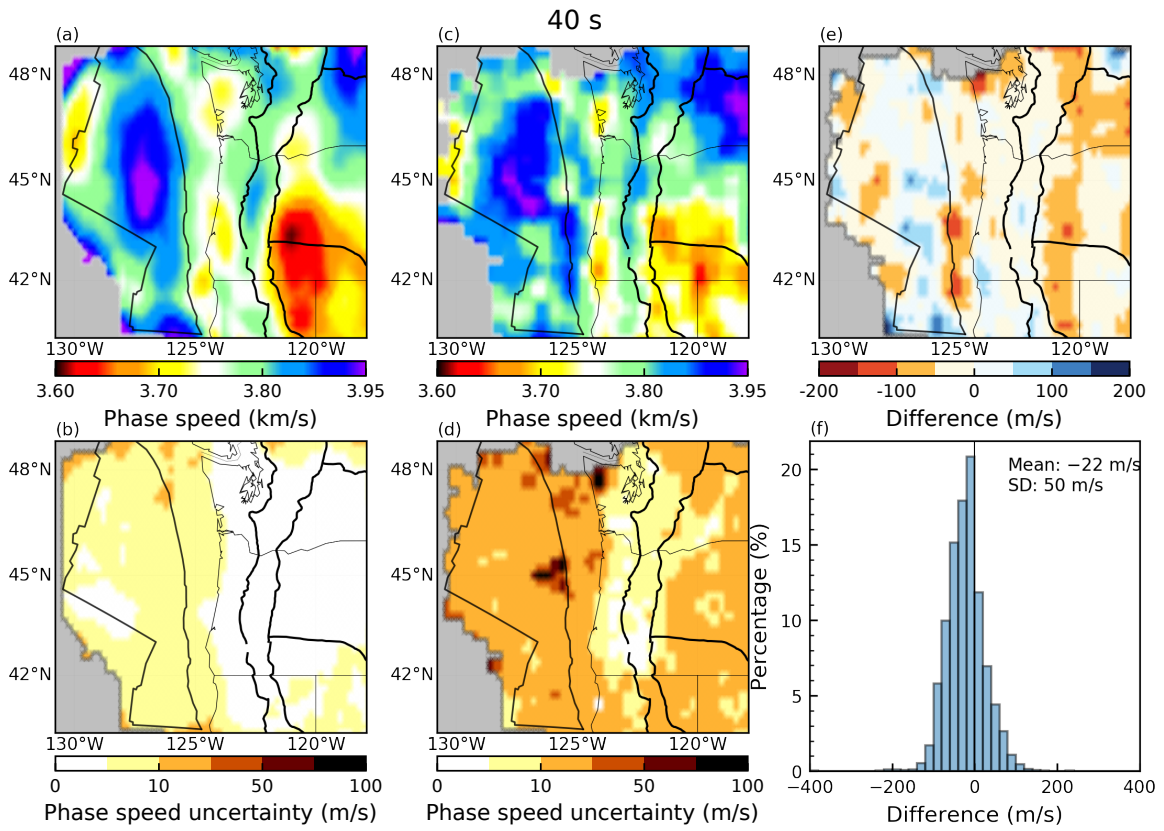


Figure S7: Same as Fig. S6 except at 40 s period.

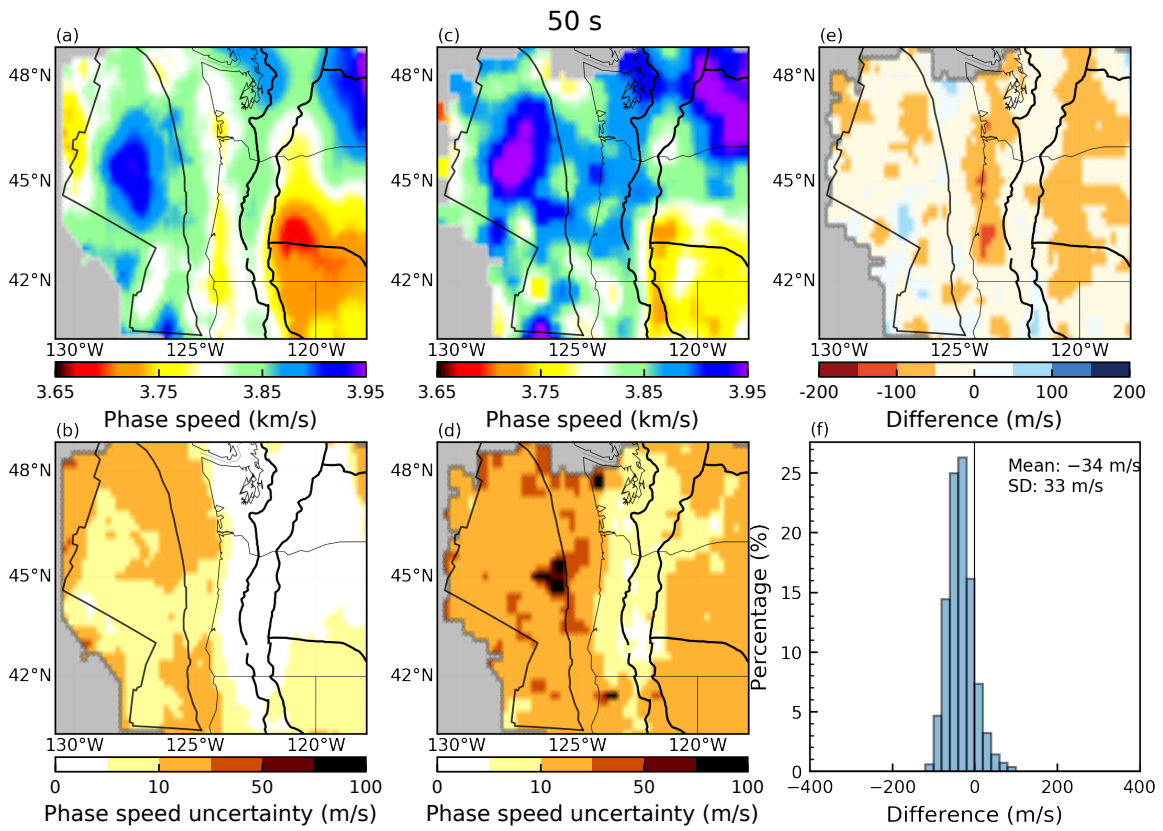


Figure S8: **Similar to Fig. S6 except at 50 s period.** (a) (b) Our results are purely based on earthquakes.

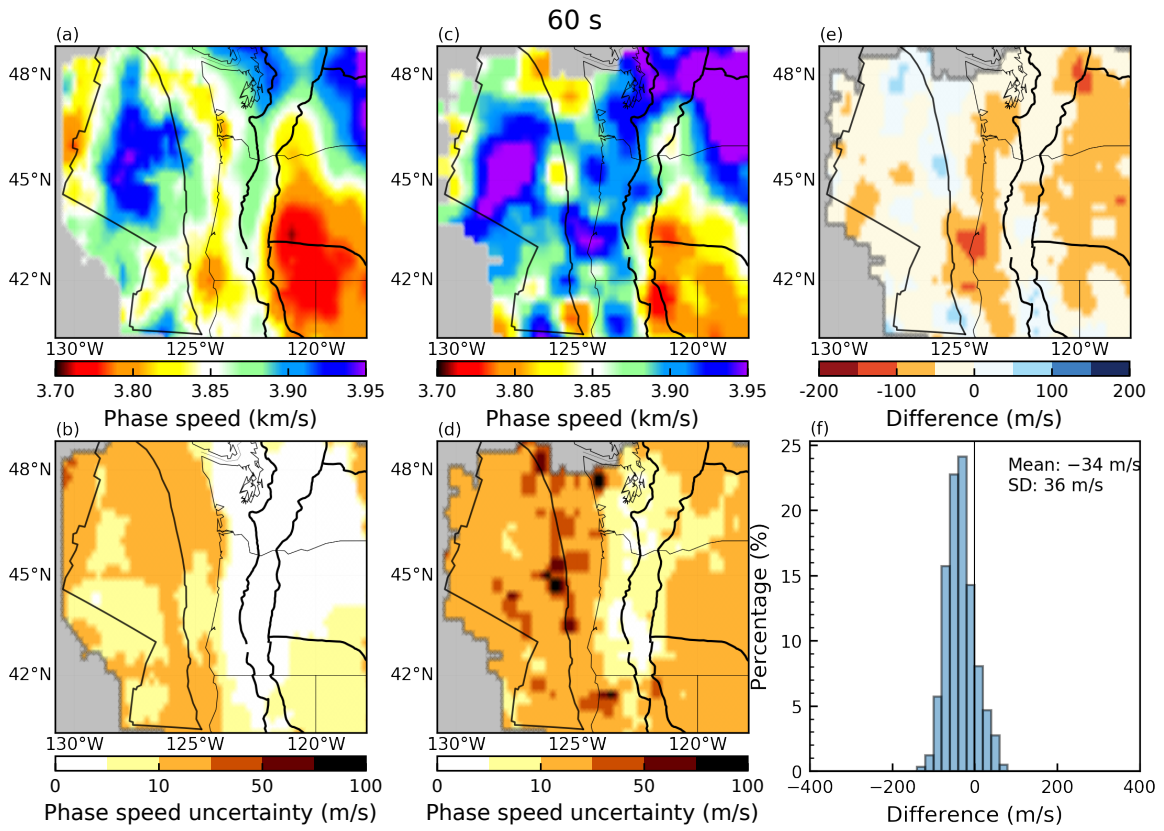


Figure S9: Same as Fig. S6 except at 60 s period.

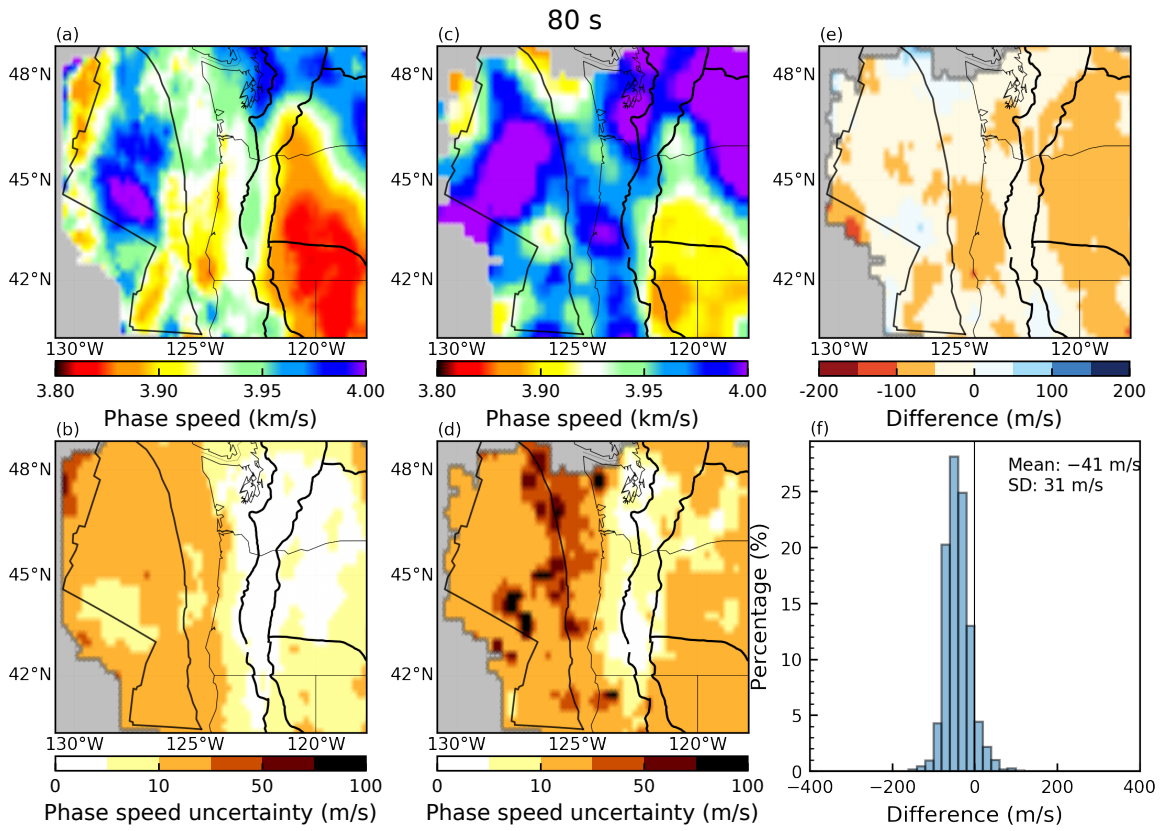


Figure S10: Same as Fig. S9 except at 80 s period.

25 **References**

- 26 Ekström, G. and M. Nettles (2018). “Observations of seismometer calibration and orientation
27 at USArray stations, 2006–2015”. *Bulletin of the seismological society of america* 108.4,
28 pp. 2008–2021. DOI: [10.1785/0120170380](https://doi.org/10.1785/0120170380).
- 29 Janiszewski, H. A., J. B. Gaherty, G. A. Abers, H. Gao, and Z. C. Eilon (2019). “Amphibious
30 surface-wave phase-velocity measurements of the Cascadia subduction zone”. *Geophysical*
31 *journal international* 217.3, pp. 1929–1948. DOI: [10.1093/gji/ggz051](https://doi.org/10.1093/gji/ggz051).